AFRL-AFOSR-UK-TR-2023-0031

High-fidelity numerical simulation of hypersonic three-dimensional shock/boundary layer interactions

Pirozzoli, Sergio
UNIVERSITA' DEGLI STUDI DI ROMA LA SAPIENZA
PIAZZALE ALDO MORO 5
ROMA, , 00185
ITA

12/13/2022
Final Technical Report

Air Force Research Laboratory
Air Force Office of Scientific Research
European Office of Aerospace Research and Development
Unit 4515 Box 14, APO AE 09421

REPORT DOCUMENTATION PAGE

PLEASE DO NOT RETURN YOUR FORM TO THE ABOVE ORGANIZATION.

1. REPORT DATE	2. REPORT TYPE	3. DATES COVERED	
20221213	Final	START DATE 20190715	END DATE 20220714

4. TITLE AND SUBTITLE
High-fidelity numerical simulation of hypersonic three-dimensional shock/boundary layer interactions

5a. CONTRACT NUMBER	5b. GRANT NUMBER	5c. PROGRAM ELEMENT NUMBER
	FA9550-19-1-7029	
5d. PROJECT NUMBER	**5e. TASK NUMBER**	**5f. WORK UNIT NUMBER**

6. AUTHOR(S)
Sergio Pirozzoli

7. PERFORMING ORGANIZATION NAME(S) AND ADDRESS(ES)
UNIVERSITA' DEGLI STUDI DI ROMA LA SAPIENZA
PIAZZALE ALDO MORO 5
ROMA 00185
ITA

8. PERFORMING ORGANIZATION REPORT NUMBER

9. SPONSORING/MONITORING AGENCY NAME(S) AND ADDRESS(ES)	10. SPONSOR/MONITOR'S ACRONYM(S)	11. SPONSOR/MONITOR'S REPORT NUMBER(S)
EOARD UNIT 4515 APO AE 09421-4515	AFRL/AFOSR IOE	AFRL-AFOSR-UK-TR-2023-0031

12. DISTRIBUTION/AVAILABILITY STATEMENT
A Distribution Unlimited: PB Public Release

13. SUPPLEMENTARY NOTES

14. ABSTRACT
The present report summarizes the main activities carried out within the research project. The main research line focuses on the effects of a crossflow on the interaction between a turbulent boundary layer and an oblique shock. The activity relies on three sets of direct numerical simulations, with different boundary layer Mach numbers (supersonic/hypersonic conditions) and shock strengths. A statistically quasi-three-dimensional configuration is considered to isolate the crossflow effect on mean flow properties, mean turbulent stresses and large-scale unsteadiness. The numerical analysis reveals that the size of the separation bubble increases with the skew angle, as a result of both earlier flow detachment and delayed reattachment. Strong non-equilibrium conditions are observed after reattachment, where the flow relaxes towards a zero-pressure-gradient state. In this region, standard gradient viscosity hypothesis fails in predicting the mean turbulent stresses, and the mean flow direction strongly deviates from the inviscid solution. Those effects appear to be more severe in the supersonic flow case, than in the hypersonic one. The supersonic flow cases present evidence, for large enough domain widths, of spanwise large-scale rippling of the instantaneous flow separation line. These ripples are advected in the spanwise direction at a fraction of the mean spanwise velocity component; their wavelength scales fairly well with the mean separation length. Based on these results, a predictive formula of the frequency band of large-scale unsteadiness with the skew angle is obtained. In agreement with the literature, it is found that the typical frequency increases with the skew angle. A parallel research activity deals with the assessment of turbulent inflow conditions for the simulations of supersonic and hypersonic boundary layers. Two main classes of inflow conditions, based on recycling/rescaling (RR) and digital filtering (DF) approaches, are considered. A series of DNS using very long streamwise domains is also performed to provide reliable benchmark data for the subsequent investigation. Simulations using shorter domains, with extent comparable with that used in the current literature, are then carried out and compared with the benchmark data. A small set of diagnostic parameters is used to verify achievement of an equilibrium state. It is found that, in the supersonic cases, RR method outperform DF in the evaluation of inner-scaled wall pressure fluctuations and turbulent shear stress. DF methods yield superior performance in predicting wall friction and streamwise Reynolds stress, at the cost of unrealistically large wall pressure variance. Simple modification of DF methods is proposed to partially handle this issue. Similar distribution of wall friction and heat transfer are instead obtained by the two baseline methods for the hypersonic case.

15. SUBJECT TERMS

16. SECURITY CLASSIFICATION OF:			17. LIMITATION OF ABSTRACT	18. NUMBER OF PAGES
a. REPORT U	b. ABSTRACT U	c. THIS PAGE U	SAR	39

19a. NAME OF RESPONSIBLE PERSON	19b. PHONE NUMBER *(Include area code)*
DOUGLAS SMITH	314 235 6013

FINAL PERFORMANCE REPORT

Grant: FA9550-19-1-7029

"High-fidelity numerical simulation of hypersonic three-dimensional shock/boundary layer interactions"

PI: Sergio Pirozzoli

Period of Performance: 15 July 2019 - 14 July 2022

Contact point: Sergio Pirozzoli
+39-06-44585202
Sapienza University of Rome
Department of Mechanical and Aerospace Engineering
Via Eudossiana 18
00184, Roma (Italy)

Summary

The present report summarizes the main activities carried out within the research project. The main research line focuses on the effects of a crossflow on the interaction between a turbulent boundary layer and an oblique shock. The activity relies on three sets of direct numerical simulations, with different boundary layer Mach numbers (supersonic/hypersonic conditions) and shock strengths. A statistically quasi-three-dimensional configuration is considered to isolate the crossflow effect on mean flow properties, mean turbulent stresses and large-scale unsteadiness. The numerical analysis reveals that the size of the separation bubble increases with the skew angle, as a result of both earlier flow detachment and delayed reattachment. Strong non-equilibrium conditions are observed after reattachment, where the flow relaxes towards a zero-pressure-gradient state. In this region, standard gradient viscosity hypothesis fails in predicting the mean turbulent stresses, and the mean flow direction strongly deviates from the inviscid solution. Those effects appear to be more severe in the supersonic flow case, than in the hypersonic one. The supersonic flow cases present evidence, for large enough domain widths, of spanwise large-scale rippling of the instantaneous flow separation line. These ripples are advected in the spanwise direction at a fraction of the mean spanwise velocity component; their wavelength scales fairly well with the mean separation length. Based on these results, a predictive formula of the frequency band of large-scale unsteadiness with the skew angle is obtained. In agreement with the literature, it is found that the typical frequency increases with the skew angle. A parallel research activity deals with the assessment of turbulent inflow conditions for the simulations of supersonic and hypersonic boundary layers. Two main classes of inflow conditions, based on recycling/rescaling (RR) and digital filtering (DF) approaches, are considered. A series of DNS using very long streamwise domains is also performed to provide reliable benchmark data for the subsequent investigation. Simulations using shorter domains, with extent comparable with that used in the current literature, are then carried out and compared with the benchmark data. A small set of diagnostic parameters is used to verify achievement of an equilibrium state. It is found that, in the supersonic cases, RR method outperform DF in the evaluation of inner-scaled wall pressure fluctuations and turbulent shear stress. DF methods yield superior performance in predicting wall friction and streamwise Reynolds stress, at the cost of unrealistically large wall pressure variance. Simple modification of DF methods is proposed to partially handle this issue. Similar distribution of wall friction and heat transfer are instead obtained by the two baseline methods for the hypersonic case.

1. Introduction

Shock-wave/turbulent-boundary-layer interactions (SBLIs) constitute a typical feature of several high-speed aerodynamic flows. Common examples of SBLI can be found in external flows, such as transonic/supersonic airfoils, aerodynamic appendices, wing-body junctions, as well as in internal flows, such as engine supersonic inlets and turbines (Smits & Dussauge, 2006). More generally, SBLIs can be found whenever a shock wave sweeps across a turbulent boundary layer developing on a solid surface. Shock impingement on a boundary layer often results in extensive flow separation, which may lead to significant performance drawback. Loss of efficiency of aerodynamic surfaces, structural vibrations triggered by wall pressure fluctuations, localized heat transfer peaks are typical examples of unwanted phenomena caused by SBLI. For this reason, this flow feature has been extensively investigated, as reported by several reference papers (Dolling, 2001; Babinsky & Harvey, 2011; Clemens & Narayanaswamy, 2014; Gaitonde & Adler, 2022).

Most experimental and numerical works are focused on a simplified two-dimensional configuration, in which the shock impingement is perfectly orthogonal to the main stream. A peculiar feature of this flow setup is the presence of large-scale unsteadiness of the separated region, which leads to intense low-frequency tones in the frequency spectra of wall pressure fluctuations around the mean separation position. The general consensus is that two main driving mechanics are responsible for low-frequency unsteadiness, as outlined by Clemens & Narayanaswamy (2014). For mildly separated flow, unsteadiness is mainly linked to advection of large-scale structures embedded in the incoming boundary layer ('upstream mechanism', see e.g. Humble *et al.*, 2009; Ganapathisubramani *et al.*, 2009). For strongly separated flows, periodic expansion and contraction resulting in 'breathing' of the separation bubble is believed to play a major role ('downstream mechanism', see e.g. Piponniau *et al.*, 2009; Touber & Sandham, 2009). Based on existing SBLI data, Dussauge *et al.* (2006) derived a scaling law for low-frequency oscillation in case of strong interactions. Specifically, they showed that the typical frequency scale with the size of the separation bubble (say, L_{sep}), and with the upstream velocity (u_0), resulting in typical Strouhal numbers $St_L = fL_{\mathrm{sep}}/u_0 \approx 0.03 - 0.05$.

However, most engineering applications are characterized by more geometrically complex kinds of interaction, in which the shock impingement line is not orthogonal to the incoming boundary layer flow. Flows over swept compression ramps (Erengil & Dolling, 1993; Settles *et al.*, 1980; Adler & Gaitonde, 2018; Vanstone *et al.*, 2017; Adler & Gaitonde, 2020), around sharp fins (Schmisseur & Dolling, 1994; Gaitonde *et al.*, 1999; Arora *et al.*, 2019), and swept impinging oblique SBLI (Doehrmann *et al.*, 2018; Padmanabhan *et al.*, 2021) are examples of three-dimensional SBLI. These interactions are more complicated than their two-dimensional counterpart from the presence of a crossflow with respect to the shock impingement line, and by the fact that the separation bubble is of open type, in contrast with the case of 2-D interactions in which separation streamlines must be closed.

Depending on the shock strength and the sweep angle, the flow can be characterized by cylindrical or conical symmetry, namely the interaction is characterized by either parallel or diverging separation/reattachment lines along the spanwise direction (Settles *et al.*, 1980). The increased geometrical complexity and difficulty to get converged statistics constitute a major issue for the investigation of three-dimensional SBLI, as only few studies (Zuo *et al.*, 2019; Fang

et al., 2017; Adler & Gaitonde, 2018, 2019, 2020) can be found in literature. As regards low-frequency unsteadiness in 3D SBLI, all of the above studies agree on an increase of the typical frequency with the sweep angle. However, whereas early experimental studies (Erengil & Dolling, 1993) suggested a continuous increasing trend with the sweep angle, recent numerical studies (Adler & Gaitonde, 2020) rather seem to indicate suppression of the low-frequency peak in the presence of three-dimensional effects, on account of a topological change of the separation bubble from a closed to an open type. Another important issue in swept interactions is the possible variation of the typical frequencies along the spanwise direction. Whereas Erengil & Dolling (1993) suggested a spanwise decrease of the typical frequencies, more recent studies tend to support invariance (Adler & Gaitonde, 2020; Padmanabhan *et al.*, 2021).

Further research on this topic is thus required to improve understanding of the underlying physical mechanisms in swept SBLI. In this respect, researchers have recently attempted to overcome the complexity of three-dimensional SBLI by considering surrogate models. The arguably simplest configuration which can be used at this aim is the interaction between a swept oblique shock wave and a fully-developed flat plate boundary layer. Both experimental (Padmanabhan *et al.*, 2021) and numerical works (Lee & Gross, 2021) have recently dealt with this setup: the former study used a swept shock generator to introduce a shock wave that is not orthogonal to the boundary layer mean flow direction, whereas the aforementioned numerical investigation employs a skewed inlet condition for the boundary layer to generate a three-dimensional interaction (2D/3C - two-dimensional, three-component - flow). These solutions appear to be very promising ways to obtain valuable information about the effect of sweep angle on the mean properties and the spectral flow behaviour in swept SBLI.

A critical feature in the numerical setup for the simulation of high-speed flow is the choice of the inflow conditions. The current state-of-the-art modeling of inlet fluctuations is generally based on two classes of numerical methods: recycling-rescaling (RR) methods (Lund *et al.*, 1998; Xu & Martin, 2004) and digital filtering (DF) methods (Klein *et al.*, 2003). It is well known that both the wall-normal distribution of the mean flow (Adler *et al.*, 2018) and the turbulent fluctuation generation (Dhamankar *et al.*, 2018) imposed at the inflow section can affect the time-averaged data obtained by the simulation. Both numerical and experimental works highlighted the need of taking flow measurements far away from the inflow section (Erm & Joubert, 1991; Simens *et al.*, 2009). In numerical simulations, this would lead to employing very long streamwise domains, which can be unacceptable for industrial applications.

Several previous studies have therefore attempted to define an inflow length, namely the minimal distance from the inflow at which the flow properties become independent of the inflow forcing (Schlatter *et al.*, 2010*a*). Wenzel *et al.* (2018) revealed that the streamwise length necessary to reach fully-developed turbulence increases monotonically as the freestream Mach number is increased, as also confirmed by Huang *et al.* (2022) for higher Mach numbers. The latter authors also noticed significant differences of numerical results obtained with the digital filtering and with the recycling/rescaling procedure, especially regarding the wake region of the boundary layer. As these problems result in relatively large scatter between similar simulations, carried out at the very same flow conditions but with different inflow strategies, the problem of inflow effects on numerical simulations of high-speed wall-bounded flows must be quantitatively assessed.

The research project aims at providing information about the effect of crossflow on sta-

tistically two-dimensional SBLI using the previously introduced 2D/3C approach. In this setup, the upstream boundary layer flow is swept by an angle γ_0 at the inflow section, hence the nominal shock impingement line is not orthogonal to the incoming flow. This configuration, hereafter referred to as skewed SBLI (SSBLI), facilitates direct comparison between two-dimensional and swept SBLIs by isolating the effects of the crossflow, at limited computational effort as compared to a fully three-dimensional study. Direct numerical simulations of skewed SBLI are carried out, both for supersonic and hypersonic incoming flow conditions. In particular, the mean flow properties of the interaction, the mean turbulent stresses and the overall flow topology are investigated for both sets of simulations. The effects of crossflow on low-frequency oscillations is also addressed with reference to the supersonic case. To avoid subtle effects of the periodic boundary conditions enforced on spanwise domain boundaries, an extensive analysis of the effect of the spanwise domain size on the spectral flow features is performed.

A parallel research line deals with the assessment of inflow effects on numerical simulations of high-speed boundary layers. The goal of this study is threefold. First, we aim at setting up a standardized procedure to evaluate achievement of equilibrium conditions in the numerical simulation of high-speed boundary layers. Second, and related to the previous item, we aim at developing a benchmark database to be used for the evaluation of the performance of inflow feeding techniques, which is devoid from inflow history effects, Third, we aim at developing improved versions of recycling-rescaling method and digital filtering.

2. Methods, Assumptions and Procedures

2.1 Conservation equations and numerical method

The numerical simulations presented in this report rely on the numerical solution of the conservation equations for mass, momentum, and energy of a compressible fluid, which read

$$\frac{\partial \rho}{dt} + \nabla \cdot (\rho \mathbf{u}) = 0, \tag{1.1}$$

$$\frac{\partial \rho \mathbf{u}}{dt} + \nabla \cdot (\rho \mathbf{u}\mathbf{u}) = -\nabla P + \nabla \cdot \overline{\overline{\tau}}, \tag{1.2}$$

$$\frac{\partial \rho e_0}{dt} + \nabla \cdot (\rho e_0 \mathbf{u}) = \nabla \cdot \left(\overline{\overline{\tau}} \mathbf{u} + \lambda \nabla T - P\mathbf{u} \right). \tag{1.3}$$

In this formulation, ρ, P, and T are the density, pressure, and temperature of the gas, respectively, and $\mathbf{u}$ is the flow velocity vector field. The total energy per unit of mass of the gas is defined as $e_0 = e + \mathbf{u} \cdot \mathbf{u}/2$, where $e = 1/\left(\gamma_g - 1\right) \mathrm{R}T$ is the internal energy per unit mass, $\gamma_g = 1.4$ is the ratio of the heat capacities of the gas, R is the gas constant. The system of equations is supplemented with the ideal gas equation of state

$$P = \rho \mathrm{R} T. \tag{1.4}$$

The local shear stress of the fluid is computed with the constitutive relation

$$\overline{\overline{\tau}} = \mu \left[\nabla \mathbf{u} + \nabla \mathbf{u}^T - 2 \left(\nabla \cdot \mathbf{u} \right) \overline{\overline{I}}/3 \right], \tag{1.5}$$

where μ is the local dynamic viscosity and $\overline{\overline{I}}$ is the identity tensor. The dynamic viscosity of the mixture is evaluated using the power law $\mu = \mu_0 \left(T/T_0\right)^{0.76}$, whereas the thermal conductivity λ is computed using a constant Prandtl number $Pr = 0.72$.

The Navier-Stokes equations are solved using the in-house high-fidelity code STREAmS (Bernardini *et al.*, 2021) for direct numerical simulations of compressible wall-bounded flows. The convective fluxes are discretized by means of a hybrid scheme that combines the energy-preserving properties of a sixth-order skew-symmetric central difference scheme (Pirozzoli, 2010) with the shock capturing properties of a fifth-order weighted essentially non-oscillatory (WENO) scheme. The switch between the two methods is controlled by a modified Ducros sensor

$$\Theta = \frac{\left(\nabla \cdot \mathbf{u}\right)^2}{\left(\nabla \cdot \mathbf{u}\right)^2 + \left(\nabla \times \mathbf{u}\right)^2 + \left(u_0/\delta_0\right)^2}, \tag{1.6}$$

which is activated when $\Theta > 0.25$ for any of the points belonging to the WENO stencil. The diffusive fluxes, expanded to Laplacian form, are discretized with sixth-order central formulas, and the time advancement is carried out with a third-order Runge-Kutta scheme (Wray, 1990).

2.2 Computational setup for SSBLI

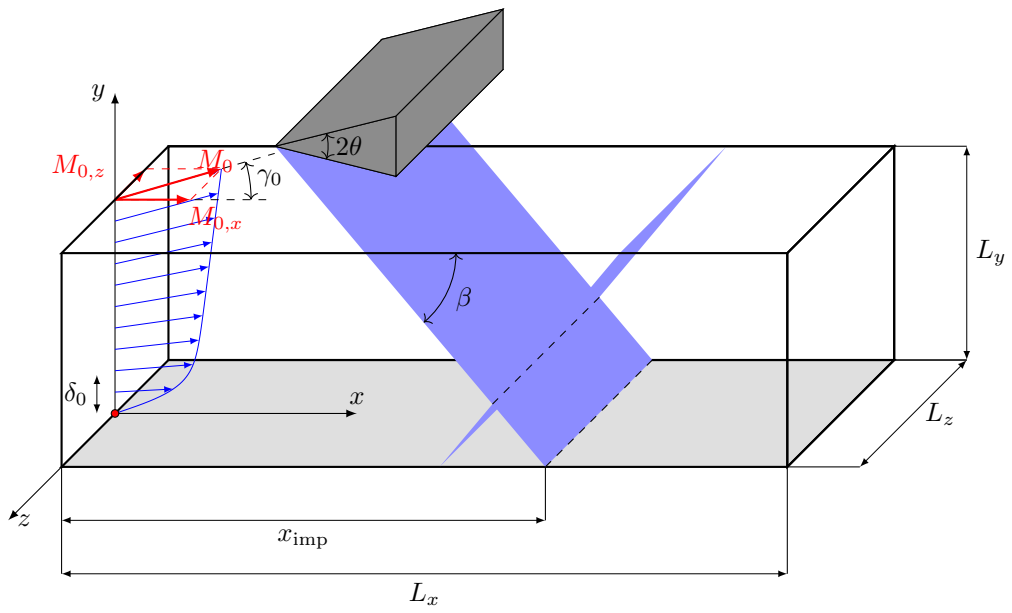

Figure 1.1: Schematic of SSBLI: γ_0 is the incoming flow skew angle; δ_0 is the incoming boundary layer thickness; β is the shock angle, θ the shock deflection angle, x_{imp} the nominal location of the shock impingement.

A schematic of the flow under scrutiny for the skewed SBLI numerical campaign is provided in figure 1.1. A turbulent boundary layer with thickness δ_0 is injected at the left boundary of the computational domain ($x = 0$), and it develops over the bottom wall skewed by an angle γ_0 with respect to the positive x direction. An oblique shock spanning the z direction impinges the boundary layer with an angle β with respect to the flat plate. The velocity inflow condition

is obtained as a combination of a Van Driest-transformed incompressible Musker profile for the time-averaged field and the velocity fluctuations are obtained through recycling-rescaling or digital filtering method. The temperature fluctuation field for digital filtering is obtained from the streamwise velocity one using the strong Reynolds analogy (SRA).

The bottom wall is assumed to be isothermal, and the wall temperature is set to its nominal adiabatic value for the incoming boundary layer. Periodicity of the flow is assumed in the z direction. Different values of the spanwise width L_z are chosen, depending on the type of analysis. For the simulation of supersonic and hypersonic interactions in section 3.1.1-3.1.2 $L_z = 16\delta_0$, whereas the investigation on low-frequency oscillations in section 3.1.3 requires wider domains, up to $L_z = 96\delta_0$. Non-reflecting boundary conditions are imposed at the outlet, right boundary ($x = 96\delta_0$), to minimize numerical feedback. Nonreflecting boundary conditions are also used at the top boundary ($y = 14\delta_0$ for hypersonic cases, $y = 18\delta_0$ for supersonic ones), with the exception of a narrow zone where the incoming shock is injected into the computational domain by hard enforcement of the Rankine-Hugoniot jump relations. In all supersonic cases the nominal impingement location is kept at $x_{imp} = 64\delta_0$, reduced to $54\delta_0$ for hypersonic ones. Skew angle values range between $\gamma_0 = 0°$ and $\gamma_0 = 45°$, whereas shock angles between $\beta = 30 - 35°$ are considered for supersonic cases ($\beta = 20°$ for hypersonic ones, corresponding to the same deflection angle $\theta = 10.4°$ as the supersonic, $\beta = 35°$ case).

Flow case	M_{x_0}	M_0	γ_0	β	θ	Re_{δ_0}	$Re_{\delta_2,r}$	L_{sep}/δ_0
M2_G0_B35	2.28	2.28	0°	35°	10.4°	10000	1034	12.65
M2_G0_B30	2.28	2.28	0°	30°	5.0°	10000	1034	1.08
M2_G15_B35	2.28	2.36	15°	35°	10.4°	11000	1112	14.36
M2_G30_B35	2.28	2.63	30°	35°	10.4°	12000	1138	19.61
M2_G30_B30	2.28	2.63	30°	30°	5.0°	12000	1141	1.26
M2_G30_B35_LR	2.28	2.63	30°	35°	10.4°	8200	829	20.40
M5_G0_B20	5.0	5.0	0	20°	10.4°	50000	750	6.83
M5_G20_B20	5.0	5.32	20°	20°	10.4°	59000	750	9.01
M5_G30_B20	5.0	5.77	30°	20°	10.4°	74500	750	11.79
M2_G00_lf	2.28	2.28	0°	32.7°, 35°	8°, 10.4°	15800	1085	4.00, 12.11
M2_G7p5_lf	2.28	2.30	7.5°	35°	10.4°	15800	1090	12.61
M2_G15_lf	2.28	2.36	15°	35°	10.4°	16200	1090	13.51
M2_G30_lf	2.28	2.63	30°	32.7°, 33.8°, 35°	8°, 9.2°, 10.4°	19000	1120	5.50, 10.01, 17.42
M2_G45_lf	2.28	3.22	45°	35°	10.4°	27500	1200	47.65

Table 1.1: Main parameters of DNS flow cases: M_{x0} is the streamwise projection of the free-stream Mach number M_0, γ_0 is the incoming flow skew angle, β is the incoming shock angle, θ is the flow deflection angle imposed by the impinging shock, Re_{δ_0} is the inlet Reynolds number based on the boundary layer thickness, $Re_{\delta_2,r}$ is the Reynolds number based on the boundary layer momentum thickness at the reference location and L_{sep}/δ_0 is the normalized length of the separation bubble measured using the shear stress at the wall.

Table 1.1 provides a schematic list of the flow cases under investigation and the corresponding main parameters. In order to isolate the effect of flow skewing by retaining the same shock strength, the projected Mach number along the streamwise direction (M_{x0}) is kept constant for all simulations, and as a consequence the actual Mach number (M_0) is changing with the

sweep angle, as $M_{x0} = M_0 \cos\gamma_0$. At a first glance, one can state that varying M_0 could bring some uncertainty related to possible effects of change of the Reynolds number; this issue is addressed within the supersonic SSBLI analysis by an additional case, in which the inlet Reynolds number is decreased by 50%. Moreover, the combination of the inflow parameters allows to obtain the same values of the momentum thickness Reynolds number $\mathrm{Re}_{\delta_2,r} = \rho_0\sqrt{u_0^2 + w_0^2}\theta_r/\mu_w$ (Smits & Dussauge, 2006), at a reference location $x_r = 35\delta_0$ located just upstream of shock impingement. The discretization of the computational domain is based an on uniform grid spacing along the x and z directions, whereas a hyperbolic sine stretching is used along the wall-normal direction within the boundary layer to have a minimum spacing $\Delta y^+_{min} = 0.65$ at the wall. An uniform grid spacing is used outside of the boundary layer region. In the following, the superscript + is used to denote the normalization with the local viscous unit $\overline{\mu_w}/\left(\overline{\rho_w}u_\tau\right)$, where the $\overline{\mu_w}$ and $\overline{\rho_w}$ are the time- and spanwise averaged dynamic viscosity and density at the wall and $u_\tau = \sqrt{\overline{\tau_w}/\overline{\rho_w}}$ is the friction velocity computed with the local mean shear stress at the wall $\overline{\tau_w}$.

All the time- and spanwise-averaged results, denoted with overline symbols, presented in the following are collected by integrating in time the governing equations of about 500 δ_0/u_0, after reaching a statistically steady state condition as estimated by monitoring the spanwise-averaged location of the separation point. For the spectral analysis in section 3.1.3 a longer time window is used, exceeding $2500\delta_0/u_0$.

2.3 Computational setup for turbulent boundary layer simulations

Two reference flow cases are selected for the turbulent bondary layer simulations, one representative of supersonic flow conditions (Pirozzoli & Bernardini, 2011), and the other of hypersonic cooled walls (Zhang *et al.*, 2018). The former case refer to a Mach number $M_0 = 2$ and adiabatic wall conditions, the latter to $M_0 = 5.84$ and $T_w/T_r = 0.25$. Time and space discretization are chosen as for the SSBLI computations described above.

For both flow cases under scrutiny, two series of DNS have been carried out, one on relatively short domains, which serves to quantify effects of inflow seeding (RR- or DF-type), as compared to benchmark simulations, carried out in very long domains, which are verified to be yield to a healthy state of developed turbulence. The full list of DNS and the key computational parameters are reported in Table 1.2. It is noteworthy that the domains of 'short' RR supersonic cases match the one used by Pirozzoli & Bernardini (2011), whereas DF domains are 50% longer to reach comparable Reynolds number.

The boundary conditions enforced at the inflow plane for short simulations are discussed in the following. For long simulations, the mean profiles are obtained by applying Van Driest transformation to boundary layer profiles of the Musker families. Besides, the bottom wall is considered as isothermal, and its temperature is fixed to its nominal adiabatic value. The flow is assumed to be periodic in the z direction, and non-reflecting boundary conditions are imposed on both the top and right boundaries. For the short-domain simulations, time averages are accumulated over at least 800 and 1750 convective time units (δ_0/u_0), for the $M_0 = 2$ and $M_0 = 5.84$ flow cases, respectively. Spanwise averaging is also performed. For the long-domain simulations, at least 1450 and 1750 convective time units have been used, respectively.

Flow case	M_0	Re_{δ_0}	L_x/δ_0	L_y/δ_0	L_z/δ_0	L_z/δ_f	Δx^+	Δy_w^+	Δz^+	$N_x \times N_y \times N_z$
M2-RR	2.00	12662	106	8.3	9.6	3.6	6.4	0.6	5.4	$4160 \times 221 \times 448$
M2-DF	2.00	12662	159	8.3	9.6	3.0	6.4	0.6	5.4	$6240 \times 221 \times 448$
M2-L1	2.00	4779	310	26	32	6.4	4.3	0.6	4.4	$6144 \times 512 \times 768$
M2-L2	2.00	8230	310	26	26	5	4.2	0.6	4.0	$10240 \times 512 \times 896$
M2-L3	2.00	12662	318	16.6	19.2	3.3	5.3	0.6	4.4	$12480 \times 448 \times 896$
M5.84-RR	5.84	23152	150	10	9	2.8	8.9	0.4	8.4	$5024 \times 224 \times 320$
M5.84-DF	5.84	23152	150	10	9	2.8	8.9	0.4	8.4	$5024 \times 224 \times 320$
M5.84-L1	5.84	10650	300	20	18	3.7	3.5	0.4	3.3	$10048 \times 352 \times 640$
M5.84-L2	5.84	16788	300	20	18	3.6	5.2	0.4	4.9	$10048 \times 352 \times 640$
M5.84-L3	5.84	23152	300	20	18	3.1	7.1	0.4	6.7	$10048 \times 352 \times 640$

Table 1.2: Summary of DNS flow cases. The suffix RR denotes cases run with the recycling-rescaling procedure, and DF denotes cases run with the digital filtering procedure. The suffix L denotes benchmark simulations, run in long domains. M_0 is the free-stream Mach number, $\mathrm{Re}_{\delta_0} = \rho_0 u_0 \delta_0 / \mu_0$ is the Reynolds number based on the inflow boundary layer thickness, L_x, L_y, L_z are the domain streamwise, wall-normal and spanwise sizes, $\Delta x^+, \Delta z^+$ are the grid spacings in the wall-parallel direction, Δy_w^+ is the minimum wall-normal grid spacing, and N_x, N_y, N_z are the number of grid points, and δ_f is the outflow boundary layer thickness.

Recyling/rescaling technique

The analysis is focused on the two most common inflow turbulence techniques, namely the recycling/rescaling and the digital filtering procedure. In both cases, all inflow properties (namely density ρ, velocity u_i and pressure p) are split into mean and fluctuating parts, namely

$$\begin{aligned} \rho(0,y,z,t) &= \bar{\rho}_0(y) + \rho_0'(y,z,t) \\ u_i(0,y,z,t) &= \tilde{u}_{i_0}(y) + u_{i_0}''(y,z,t) \\ p(0,y,z,t) &= \bar{p}_0 \end{aligned} \tag{1.7}$$

where the 0 subscript is used to denote inflow quantities. In recycling/rescaling methods, the fluctuations of each flow variable are extracted at a suitable station (say x_{RR}), and recycled to the inflow plane, after suitable rescaling. The rescaling procedure is applied by dividing the boundary layer into two sub-layers: the inner layer (superscript 'inn') where velocity is assumed to scale in inner coordinates ($y^+ = y/\delta_v$), and the outer layer (superscript 'out') where flow properties scale in outer units ($Y = y/\delta$). A weight function is used to combine inner and outer fluctuations, which read

$$\varphi = \varphi^{\mathrm{inn}}(1 - W(Y)) + \varphi^{\mathrm{out}}\, W(Y), \tag{1.8}$$

with

$$W(Y) = \frac{1}{2}\left\{1 + \tanh\left[\frac{\alpha(Y-b)}{(1-2b)Y+b}\right] / \tanh\alpha\right\}, \tag{1.9}$$

and $\alpha = 4$, $b = 0.2$.

The inflow density and velocity fluctuations in each layer are rescaled from the recycling

Λ_i	u'	v'	w'
$\Lambda_{z,\mathrm{inn}}/\delta_{\nu,0}$	150	75	150
$\Lambda_{z,\mathrm{out}}/\delta_0$	0.4	0.3	0.4
Λ_x/δ_0	0.8	0.3	0.3

Table 1.3: Spanwise and streamwise integral length scales used in DF implementation for the velocity components u', v', w'. $\Lambda_{z,\mathrm{inn}}$ is the inner integral length scale, $\Lambda_{z,\mathrm{out}}$ is the outer integral length scale, and Λ_x is the streamwise length scale.

station according to

$$\begin{aligned}
\rho_0'|^{\mathrm{inn}}(y^+,z,t) &= \rho'(x_r,y^+,z+L_z/2,t),\\
u_{i0}''|^{\mathrm{inn}}(y^+,z,t) &= \gamma\, u_i''(x_r,y^+,z+L_z/2,t),\\
\rho_0'|^{\mathrm{out}}(Y,z,t) &= \rho'(x_r,Y,z+L_z/2,t),\\
u_{i0}''|^{\mathrm{out}}(Y,z,t) &= \gamma\, u_i''(x_r,Y,z+L_z/2,t),
\end{aligned} \tag{1.10}$$

where γ is the rescaling parameter, $\gamma = u_{\tau 0}/u_{\tau r}$, which we estimate as $\gamma = (\delta_r/\delta_0)^{0.13}$, Following previous studies (Pirozzoli & Bernardini, 2011), the recycling station is placed at $x_{RR} = 53\delta_0$. This baseline form of the recycling/rescaling procedure is hereafter referred to as RR1.

A possible simplification of the RR procedure considers a remapping of the wall-normal coordinate with stretching factor defined to be $\delta_{\nu,r}/\delta_{\nu,0}$ close to the wall (to achieve correct rescaling in the inner layer) and δ_r/δ_0 away from it (to achieve correct rescaling in the outer layer). A simple tanh blending of the type

$$\frac{\hat{y}}{y} = \frac{\delta_{\nu,0}}{\delta_{\nu,r}} + \frac{1+\tanh\left[\log(Y/Y_c)/\Delta\right]}{2}\left(\frac{\delta_0}{\delta_r} - \frac{\delta_{\nu,0}}{\delta_{\nu,r}}\right), \tag{1.11}$$

where $Y_c = 0.08$, $\Delta = 1.1$ is used to blend the previously defined trasformed coordinates. The fluctuations at the inflow station are then obtained as follows

$$\begin{aligned}
\rho_0'(\hat{y},z,t) &= \rho'(x_r,y,z+L_z/2,t)\\
u_{i\,0}''(\hat{y},z,t) &= \gamma u_i''(x_r,y,z+L_z/2,t).
\end{aligned} \tag{1.12}$$

This variant is hereafter referred to as RR2. Finally, we also consider a simple variant which includes remapping of the wall-normal coordinate based only on the ratio of the boundary layer thicknesses δ_r/δ_0, (hence, $\hat{y}/y = \delta_0/\delta_r$) and which is hereafter referred to as RR3.

Digital filtering technique

The digital filtering implementation relies on an extension of the technique originally introduced by Klein *et al.* (2003), which makes use of the strong Reynolds analogy (SRA) (Touber & Sandham, 2009) to generate temperature fluctuations. Specifically, synthetic velocity fluctuations are first generated from a white-noise sample, which is then filtered based on a sequence of one-dimensional convolutions, thus obtaining a correlated signal in space and time, with arbitrarily prescribable integral length- and time- scales. Different wall-normal distributions of the spanwise integral length scale (Λ_z) are assigned for each velocity component. Following

Xie & Castro (2008), two length scales are used for the inner ($\Lambda_{z,\mathrm{inn}}$) and for the outer ($\Lambda_{z,\mathrm{out}}$) wall layer, which are suitably blended to give

$$\Lambda_z(y) = \Lambda_{z,\mathrm{inn}} + (\Lambda_{z,\mathrm{out}} - \Lambda_{z,\mathrm{inn}}) \frac{1 + \tanh\left[(y/\delta_0 - 0.2)/0.03\right]}{2}. \tag{1.13}$$

For the low Reynolds numbers involved in the present analysis the outer length scale is selected throughout. Values of the integral length scales are reported for each velocity component in table 1.3. As reported by Xie & Castro (2008), the digital filtering technique has rather small sensitivity to variations in the integral length scales.

The wall-normal integral length scales are then selected as $\Lambda_y(y) = 0.67\Lambda_z(y)$. Finally, constant values of the longitudinal integral length scales Λ_x are assigned for each velocity component as in Table 1.3. The streamwise length scales are then converted to time scales using Taylor hypothesis. The resulting velocity fluctuations are then rescaled to match a desired wall-normal distribution of Reynolds stresses. This baseline implementation of the DF algorithm is hereafter referred to as DF1.

Modifications of the baseline DF algorithm are also considered in the present work. In preliminary attempts of improving the performance of DF, we found that removing the streamwise velocity fluctuations at the inflow yields reduction of spurious pressure disturbances generated by the DF1 implementation. This variant is referred to as DF2 in the following. A further improvement includes introducing a suitable streamfunction for the cross-stream velocity fluctuations to make the inflow turbulence solenoidal. The streamfunction is defined such as

$$v' = \frac{\partial \Psi'}{\partial z}, \quad w' = -\frac{\partial \Psi'}{\partial y}, \tag{1.14}$$

and we assume

$$\Psi'(y, z, t) = C(y)\, r(y, z, t), \tag{1.15}$$

where $r(y, z, t)$ is obtained from application of a low-pass filter to a white-noise generator, and $C(y)$ is a suitable scaling function. The cross-stream velocity fluctuations are then obtained from equation (1.14). The shape of the scaling function is chosen so as to achieve a prescribed distribution of the wall-normal Reynolds stress,

$$\overline{v'v'} = \overline{\frac{\partial \Psi'}{\partial z}\frac{\partial \Psi'}{\partial z}} = C^2(y)\overline{\frac{\partial r}{\partial z}\frac{\partial r}{\partial z}}. \tag{1.16}$$

It is noteworthy that the variance term at the right-hand-side of (1.16) can be computed beforehand, depending only on the spanwise length scale Λ_z in this formulation. As the present method hard enforces the distribution of the wall-normal velocity variance, the spanwise variance cannot be controlled independently to fit the target distribution. This variant is referred to as DF3 in the following.

3. Results and Discussion

3.1.1 Supersonic SSBLI

Figure 1.2 depicts instantaneous streamwise velocity fields in a wall-parallel plane extracted at $y_r^+ = 6.5$ for flow cases with different shock strength and skew angle. Upstream of the

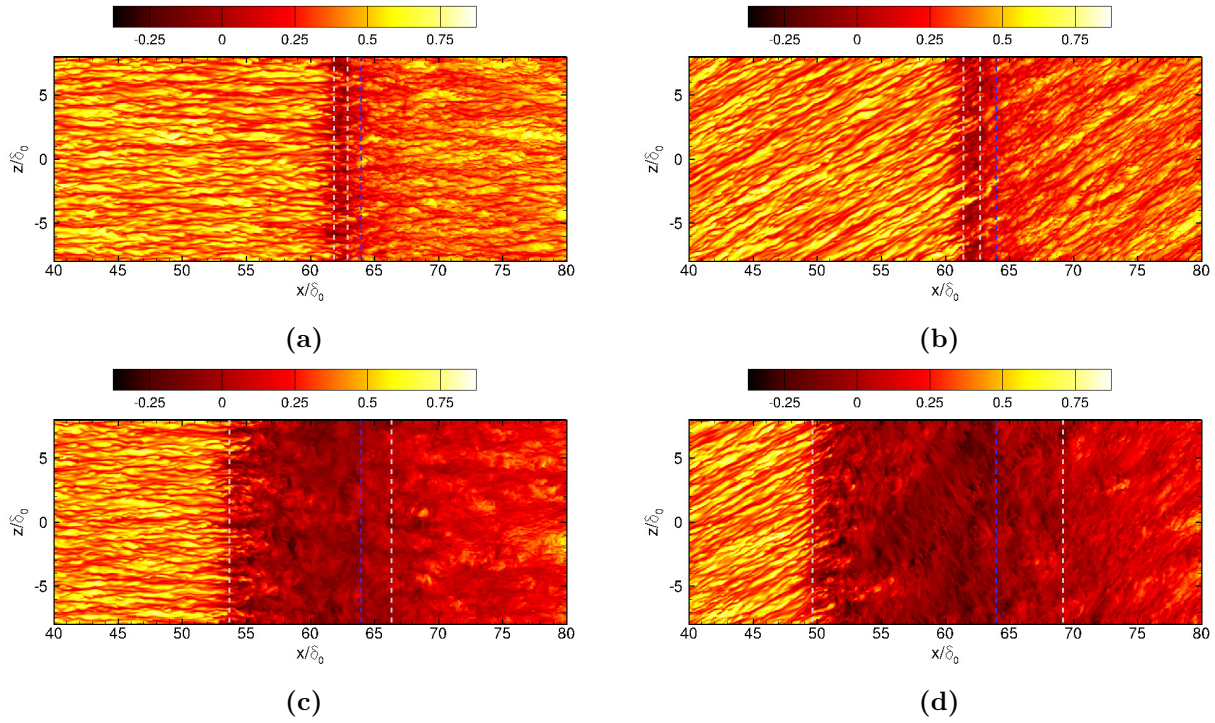

Figure 1.2: Contour plots of streamwise velocity in wall-parallel planes ($y_r^+ = 6.5$) for flow cases G0_B30 (a), G30_B30 (b), G0_B35 (c), G30_B35 (d). The dashed gray lines denote the average separation and reattachment positions. The dashed blue line denotes the location of the inviscid shock impingement.

interaction zone, the velocity field is organized into well-ordered streaks aligned with the mean flow direction. Figure 1.2 (b,d) clearly show that the incoming flow is not orthogonal to the interaction zone, whose boundaries are obtained as the mean separation and reattachment lines (in terms of time-average skin friction). As expected, cases with stronger shock (Figure 1.2 (c,d)) feature a larger separation bubble. More interestingly, the presence of a skew angle between the boundary layer and the crossflow tends to modify the dimensions of the separation bubble, which is found to be larger for the skewed cases. The flow topology in the interaction zone is characterized by convergence of friction lines towards the separation line, and divergence from the reattachment line. Streamwise streaks are destroyed within the separation zone, and the flow reorganizes itself again in streaks in the recovery region past reattachment. Flow equilibrium is rapidly attained for the weaker shock cases, whereas the flow is still far from equilibrium at the outflow boundary for the stronger shock cases.

The mean flow characteristics are investigated by means of friction coefficient, local mean flow direction and principal directions of the turbulent stress tensor. Figure 1.3 reports variation of the friction coefficient projected along the x direction, $C_{f,x} = 2\mu_w(\partial\overline{u}/\partial y)|_w/(\rho_0 u_0^2)$. The interaction zone is characterized by negative values of the projected friction coefficient, and it is followed by a relaxation region characterized by larger C_f values. The figure confirms the increasing trend of the separation zone size with γ_0, clearly visible for the strongest shock case, both due to advanced separation and delayed reattachment. A nonlinear effect of γ_0 on

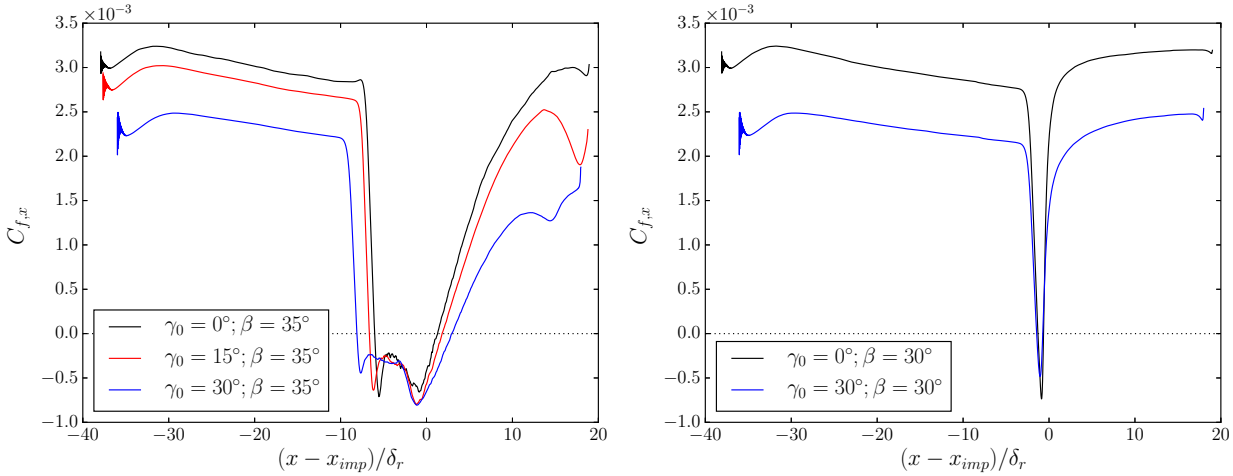

(a) **(b)**

Figure 1.3: Distribution of friction coefficient projected along the x direction for flow cases with shock angle $\beta = 35°$ (a) and $\beta = 30°$ (b).

the separation size is retrieved, as the case with $\gamma_0 = 15°$ yields an increase of about 13% in the extent of the separated flow, whereas $\gamma_0 = 30°$ yields a 47% increase. The effect of Reynolds number on the separated flow features appears to be negligible, as in cases G30_B35 and G30_B35_LR. DNS carried out with weaker shock ($\beta = 30°$) yield much smaller separation bubbles, and are much less affected by crossflow effect.

Information on the flow unidirectionality can be gathered by analyzing the distribution of the local mean flow angle, measured with respect to the positive x-direction, and defined as $\gamma = \tan^{-1}(\overline{w}/\overline{u})$. Figure 1.4 shows these distributions for the stronger shock case, at different wall-parallel axes ($y/\delta_0 = 0.1$, $y = \delta$) and the friction line orientation ($y/\delta_0 \to 0$). Reversed flow regions are characterized by $\gamma > 90°$. As expected, upstream of the interaction zone γ is equal to the imposed skew angle γ_0. As the flow reaches the interaction region, the flow angle is found to vary both with the streamwise coordinate as well as with the wall distance. Whereas a step change of γ is found for the unskewed case, in the presence of a skew angle the flow in the interaction zone becomes oriented to a higher γ, as the spanwise velocity is not directly affected by deceleration across the impinging shock.

At the edge of the boundary layer, skewed flows do not immediately relax to the equilibrium direction estimated for inviscid flow, marked with dotted lines. In fact, the flow angle peaks at its inviscid value just after the flow encounters the reflected shock, namely $x \sim 60\delta_0$ in figure 1.4c. However, flow expansion occurring past the separation bubble accelerates the flow in the streamwise direction, with subsequent reduction of γ. Relaxation to the inviscid post-shock direction then follows from lower values, and it appears to be still incomplete within the computational domain for the stronger shock case. The flow direction within the boundary layer is completely different, as γ substantially overshoots its nominal inviscid value throughout the interaction zone and in the downstream relaxation zone, in which a tendency for the flow to realign with the outer direction is observed, however from larger values of γ. Overall, there is evidence for severe variation of the direction of the velocity vector across the boundary

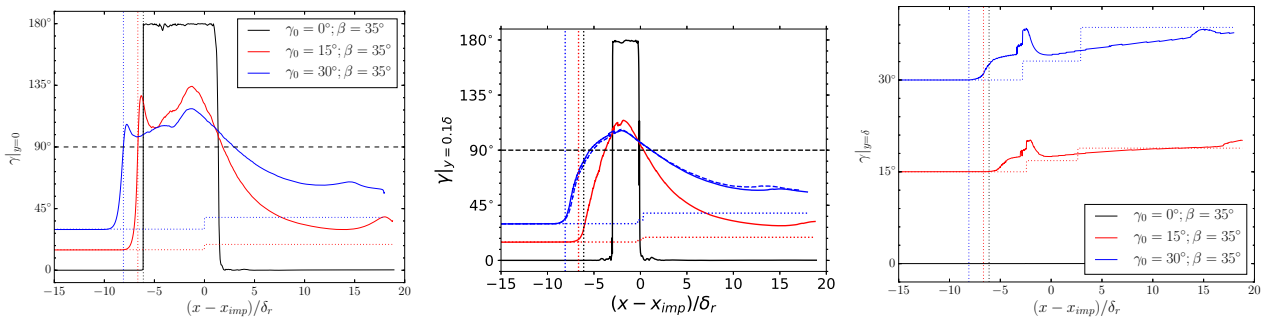

(a) **(b)** **(c)**

Figure 1.4: Distribution of mean flow angle in $x - z$ plane ($\gamma = \tan^{-1}(\overline{w}/\overline{u})$) at $y = 0$ (a,), $y = 0.1\delta$ (b), and $y = \delta$ (c) for cases with shock angle $\beta = 35°$ Dotted lines indicate the inviscid flow distributions.

layer throughout the non-equilibrium zone, which is reminiscent of the re-equilibration process observed in non-equilibrium boundary layers at low speed (Coleman *et al.*, 2019; Lozano-Durán *et al.*, 2020).

The present DNS database can be used to test the suitability of certain assumptions, largely made in the development of RANS/LES models, for the relaxation region. Most RANS models are based on the eddy-viscosity hypothesis, which states that the principal directions of the Reynolds stress tensor are aligned with the principal directions of the mean strain-rate tensor. Figure 1.5 depicts wall-normal profiles of the difference between the Reynolds stress angle $\overline{\gamma}_R$ and the strain angle $\overline{\gamma}_S$ defined as follows

$$\overline{\gamma}_R = \tan^{-1} \frac{\widetilde{\overline{\rho} v'' w''}}{\widetilde{\overline{\rho} u'' v''}} \qquad \overline{\gamma}_S = \tan^{-1} \frac{d\tilde{w}/dy}{d\tilde{u}/dy}$$

in the recovery zone. Substantial misalignment between $\overline{\gamma}_R$ and $\overline{\gamma}_S$ is observed: whereas in the outer layer their difference is overall slightly positive (hence the Reynolds stress seems to lead mean strain), it becomes largely negative next to the wall. The misalignment reduces farther downstream on account of faster relaxation of the mean strain rate. This feature can be attributed to the large characteristic time required by the Reynolds stress to adapt to the flow direction.

3.1.2 Hypersonic SSBLI

Figure 1.6 (a) depicts the streamwise distribution of the time-averaged skin friction coefficient projected along the x direction $C_{f,x}$ and the normalized mean wall pressure p_w/p_0. Similar to the supersonic cases, the main effect of the skew angle is an increase in the size of the recirculation bubble, as well as in the overall length of the interaction region (defined as the region of variation of p_w in figure 1.6 (b)).

Again, the increase of the recirculation region size is both due to early separation and delayed flow reattachment with respect to the unskewed case. The effect of the skew angle is clearly nonlinear as the variation of L_{sep} between the skewed cases is relatively bigger than the one between $\gamma_0 = 0°$ and $\gamma_0 = 20°$. A similar behaviour is also clear in figure 1.6 (b) for the

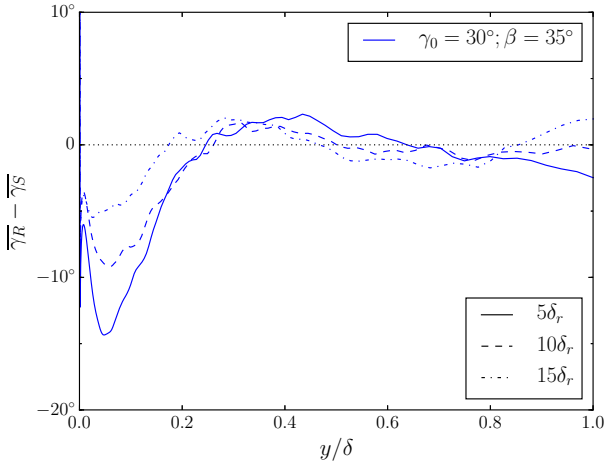

Figure 1.5: Wall-normal distribution of the misalignment between the Reynolds stresses and the mean strain, for different values of the skew angle γ_0 at three different distances from the reattachment line: $5\delta_r$ (solid lines), $10\delta_r$ (dashed), $15\delta_r$ (dash-dotted).

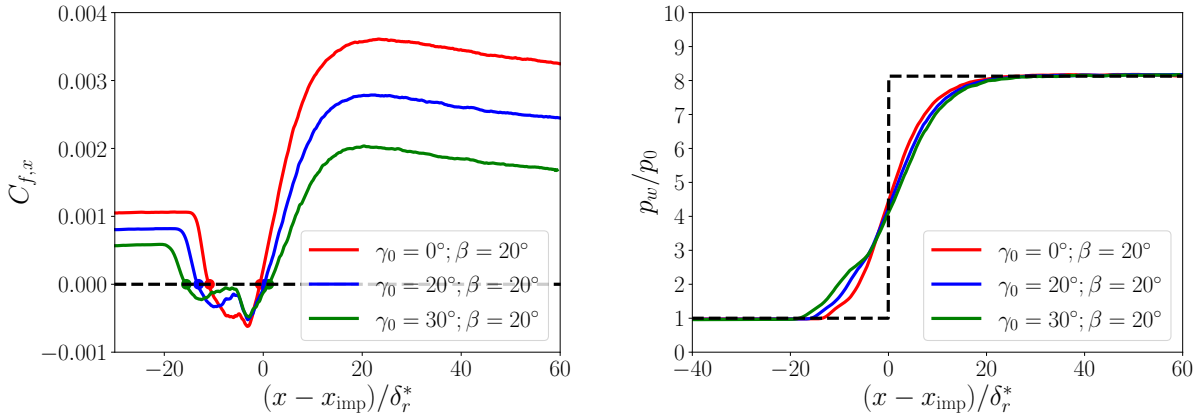

Figure 1.6: Distribution of the x-projected skin friction coefficient $C_{f,x}$ (left) and wall pressure (right) along the streamwise direction x. δ_r^* is the displacement thickness at the reference position $x_r = 35\delta_0$, x_{imp} the nominal shock impingement location. The dashed line in the p_w plot depicts the flow inviscid solution.

interaction length, which also shows that wall pressure reaches its inviscid value downstream of the impinging shock more slowly for the skewed cases. As expected, all simulations ultimately reach the inviscid value of the wall pressure predicted by Rankine-Hugoniot relations.

The wall-normal size of the separation bubble can be obtained by analyzing the dividing streamline of the bubble, reported in figure 1.7 for the three hypersonic cases. The dividing streamline is obtained by integrating the streamfunction equation from the wall until a value of $u = 0$ is obtained. The size of the bubble is clearly increasing with γ_0, mainly due to the growing streamwise extension of the interaction region. Indeed, the initial slopes of the dividing streamlines are basically the same for all cases, as the maximum deviation sustained by the flow only depends on the inlet Mach number (Babinsky & Harvey, 2011; Matheis &

Hickel, 2015).

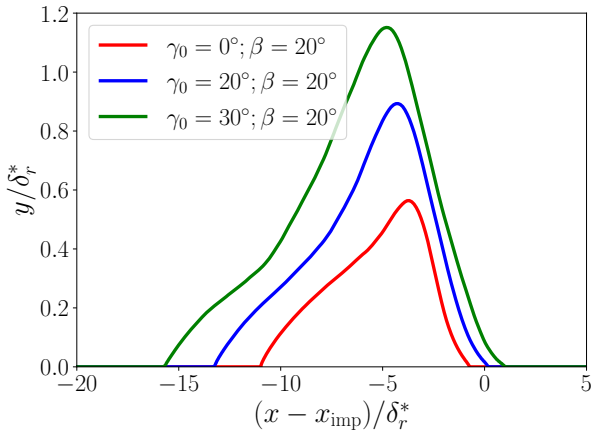

Figure 1.7: Dividing streamline of the separation bubble for different values of the skew angle γ_0.

Quantitative results about the flow direction are obtained by inspecting the time-averaged local flow angle. The angle γ_w between the local friction line direction and the x axis and the flow direction at the boundary edge $\gamma(y = \delta_{99}) = \tan^{-1}(\overline{w}/\overline{u})$ are reported in Figure 1.8, along with their corresponding inviscid solutions. In skewed cases, the flow is clearly non-unidirectional, as the local direction is $90° < \gamma < 180°$. Differently from the supersonic case, a quick recovery is observed in the post-shock region, as γ reaches the inviscid solution about $20\delta_r^*$ past reattachment. The variation of the flow angle at the boundary layer edge is smoother than the friction line angle, and features very small deviation from the inviscid solution in the interaction region.

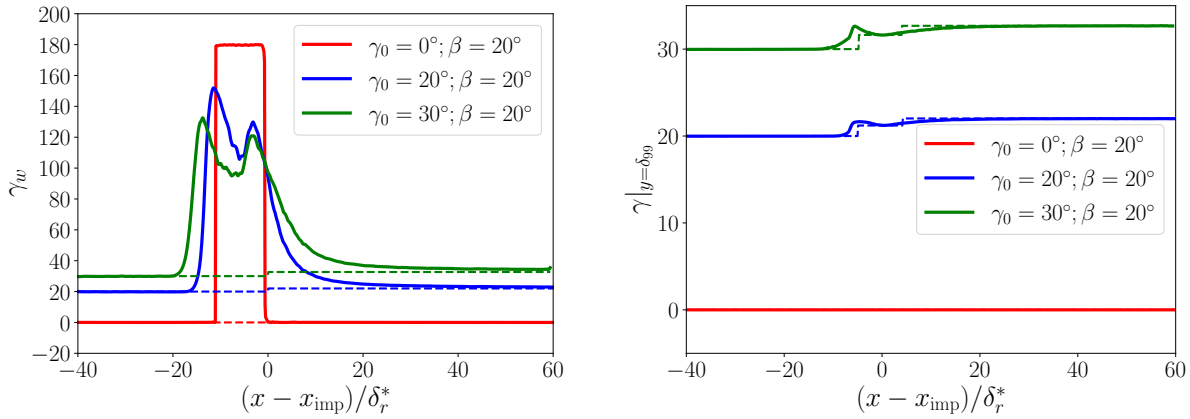

Figure 1.8: Streamwise distribution of the time-averaged flow direction at the wall γ_w (left) and at boundary layer edge $y = \delta$ (right) for different values of the skew angle γ_0 . Dashed curves indicate the inviscid γ distributions.

Finally, the effect of the skew angle on the direction of the principal axes of the Reynolds

stress tensor in the post-shock region is analyzed. Figure 1.9 highlights that a severe misalignment between γ_R and γ_S exists in the post-shock region. The misalignment is largely negative in the inner layer, and grows with the skew angle; its magnitude drops in the outer layer and while moving downstream of the reattachment line.

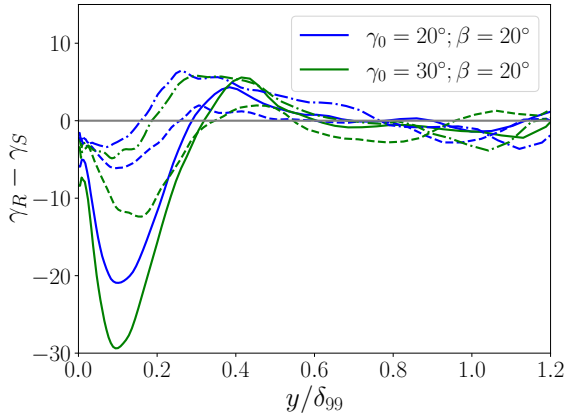

Figure 1.9: Wall-normal distribution of the misalignment between the Reynolds stresses and the mean strain, for different values of the skew angle γ_0 at three different distances from the reattachment line: $5\delta_r$ (solid lines), $10\delta_r$ (dashed), $15\delta_r$ (dash-dotted).

3.1.3 Low-frequency oscillations

After analyzing the mean properties of the SSBLI configuration, wall pressure spectra are investigated. As a preliminary step of the analysis, several numerical domains are tested to find an appropriate computational setup. In this respect, the spanwise width L_z is varied between 8 and 96 δ_0, and the effect of the spanwise width is investigated. Figure 1.10 shows that the effect of the domain width on the prevously discussed x-projected friction coefficient and the pressure variance is negligible, both in unskewed and skewed configurations.

Maps of the power spectral density (PSD) of wall pressure are shown in figure 1.11, normalized by the respective variances ($\hat{E}(f)$), in pre-multiplied form. Consistent with the general wisdom, the unswept case shows the occurrence of low-frequency dynamics at $10^{-2} \lesssim St_L \lesssim 10^{-1}$, in a limited space interval around the mean separation point. No obvious effect of the spanwise domain size is visible in that case. The swept case in small domains (panel (c)) also shows a similar pattern, on account of previously noted differences in the size of the interaction zone. Quite surprisingly, DNS of the swept case in a large domain (panel (d)) shows substantial increase of the peak frequency, which was the original motivation for further analysis.

The spatial pattern of wall pressure is then investigated through Proper Orthogonal Decomposition (POD). Figure 1.12 depicts the shape of the most energetic POD modes for $\gamma_0 = 30°$, in small and large domains, along with their associated PSD. The leading POD mode in the small domain features a spanwise-invariant distribution, with a sharp peak at mean separation line, and a flatter distribution with opposite sign at reattachment, hence overall reminiscent of bubble breathing. The PSD of the associated temporal coefficient in fact has a peak at

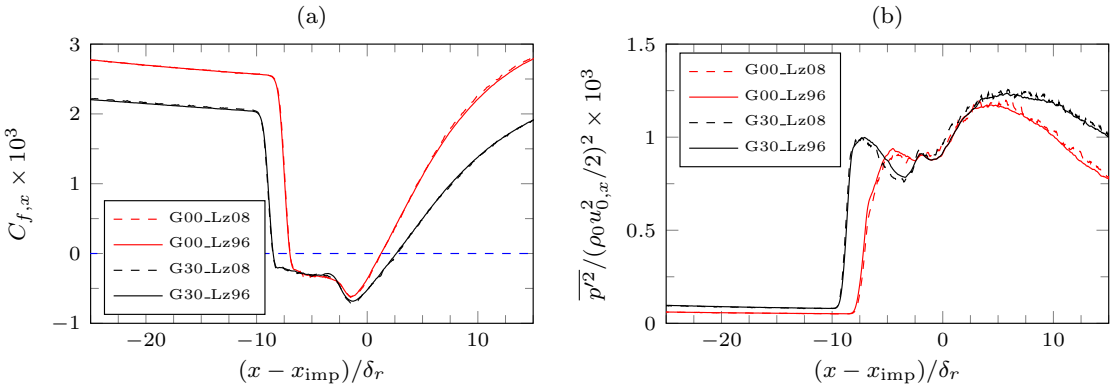

Figure 1.10: Distributions of x-projected friction coefficient (a) and wall pressure variance (b). Solid lines denote DNS in the widest domain ($L_z = 96\delta_0$), and dashed lines DNS in the narrowest domain ($L_z = 8\delta_0$). Two-dimensional cases ($\gamma_0 = 0°$) are coloured in red, and swept cases (with $\gamma_0 = 30°$) are coloured in black. The streamwise coordinate is scaled by the boundary layer thickness δ_r upstream of the mean separation line.

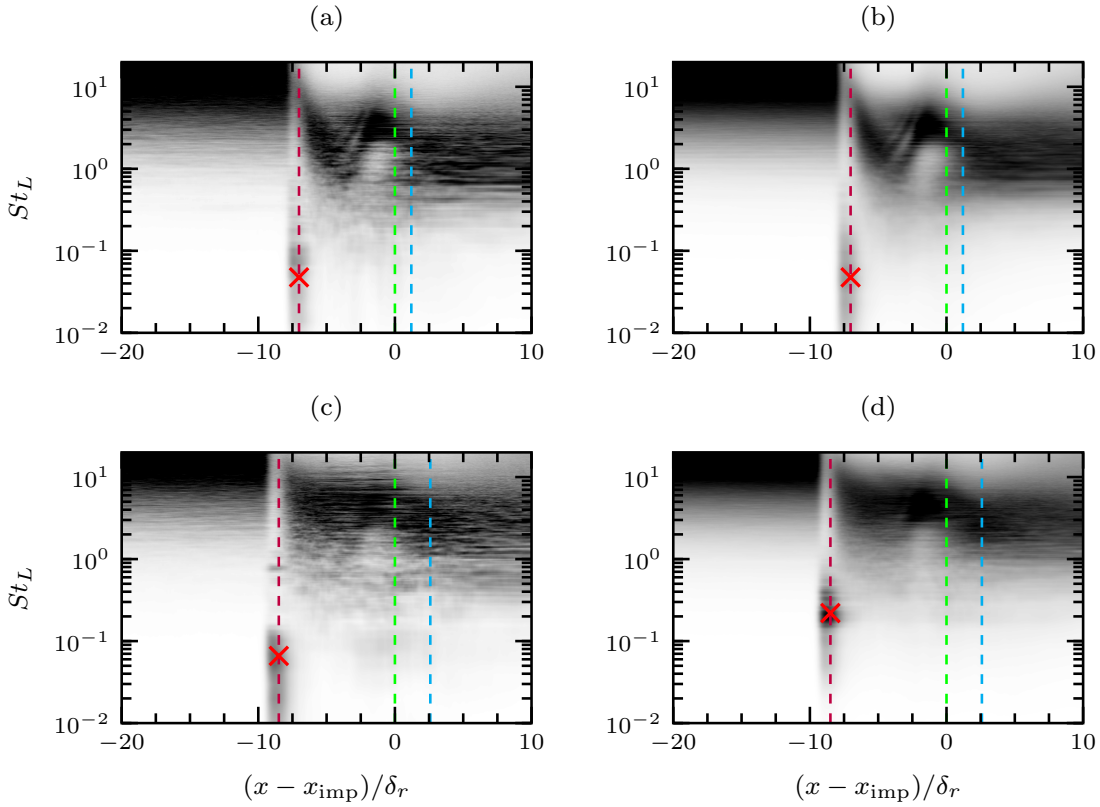

Figure 1.11: Pre-multiplied, normalized PSD of wall pressure for flow cases G00_Lz08 (a), G00_Lz96 (b), G30_Lz08 (c), G30_Lz96 (d). The purple line denotes the mean separation location, the green line the nominal shock impingement location, and the cyan line the mean reattachment location. Red crosses mark the position of the low-frequency peaks near the separation line

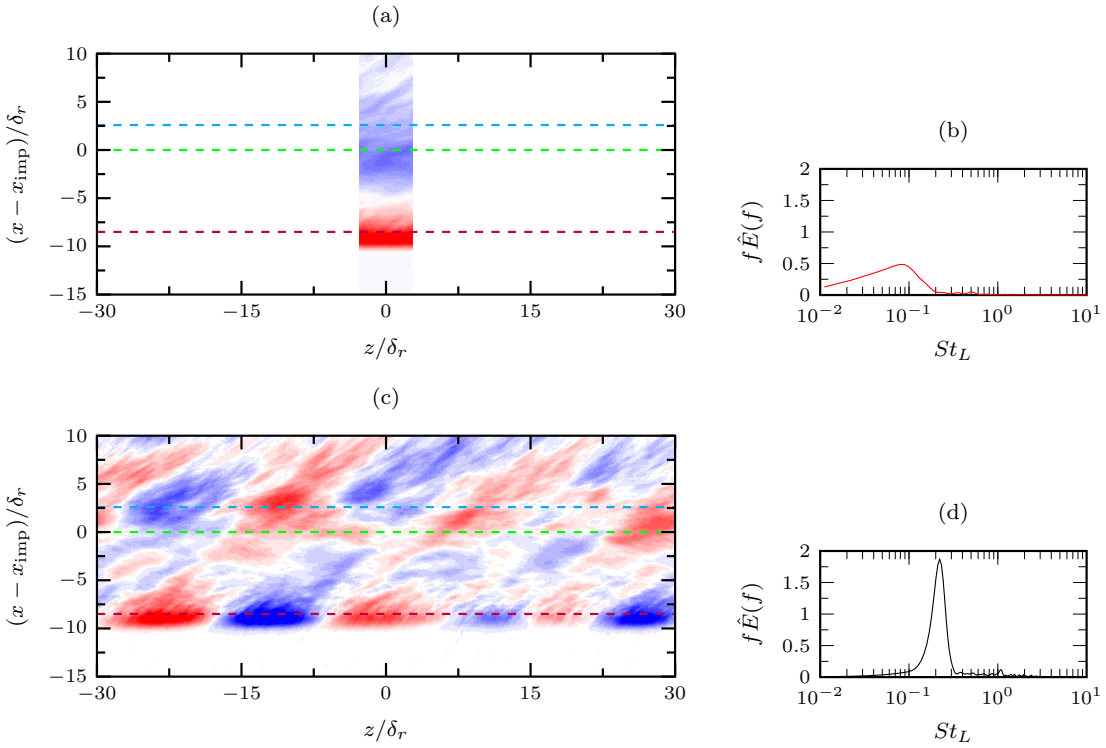

Figure 1.12: Shape of leading POD mode of wall pressure (a,c) and associated pre-multiplied, normalised PSD of the corresponding temporal coefficient (b,d). Horizontal coloured dashed lines as in figure 1.11. (a,b) $\gamma_0 = 30°$, $L_z = 8\delta_0$. (c,d) $\gamma_0 = 30°$, $L_z = 96\delta_0$.

$St_L \approx 0.07 - 0.08$, which is very close to the peak value of the pressure PSD in figure 1.11(c). The leading POD mode in the $L_z = 96\delta_0$ box is instead characterized by apparent spanwise corrugation around the mean separation line, and by oblique structures stretching up to the reattachment line. The PSD of the associated temporal coefficient peaks at $St_L \approx 0.22$, which is very close to the peak frequency of the temporal PSD at the separation line in figure 1.11(d). Similar conclusions apply to all cases under scrutiny, including unswept ones. We find that rippling of the separation line is visible only if sufficiently wide boxes are used, specifically in cases with $L_z \geq 24\delta_0$.

In order to quantitatively characterize the observed rippling of the separation line, in figure 1.13 we show the PSD of the wall pressure as a function of the spanwise wavelength, scaled either by the incoming boundary layer thickness or by the separation size. It is quite clear that better collapse of the PSD across the γ_0 range is achieved in the latter case, with possible exception of the $\gamma_0 = 45°$ case which exhibits massive flow separation and for which even the largest box used here may be marginal. Two spectral peaks are observed, one at relatively small wavelengths ($\lambda_z \approx 0.1 L_{\mathrm{sep}}$), which would probably correspond to the small-scale rippling noticed in previous numerical simulations of unswept SBLI (Pasquariello *et al.*, 2017). However, the most prominent peak resides at much longer wavelengths ($\lambda_z \approx 2L_{\mathrm{sep}}$), which cannot be resolved in numerical simulations in small boxes.

Wavenumber-frequency spectra at the mean separation line are further considered in figure

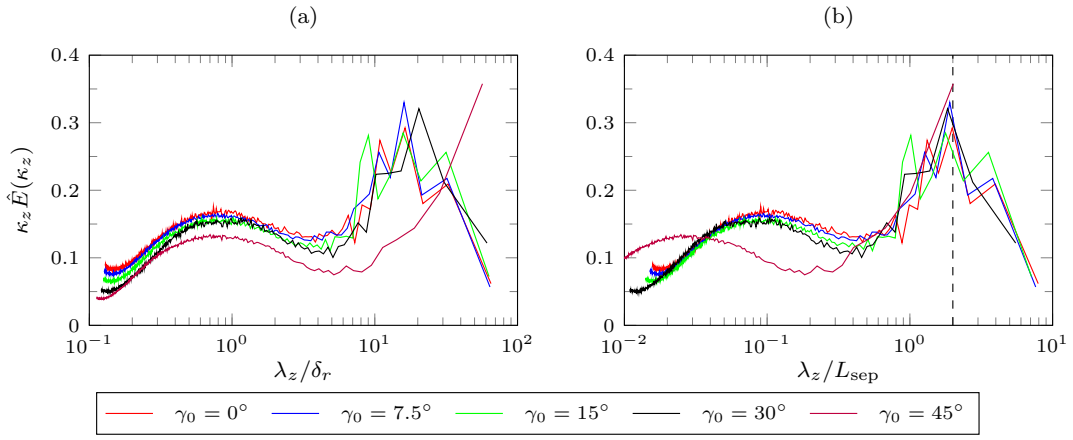

Figure 1.13: Spanwise pre-multiplied, normalised PSD of wall pressure at mean separation line for different sweep angle γ_0. The spanwise wavelength λ_z is scaled with either the reference boundary layer thickness δ_r (panel a) and the separation length (panel b). $\kappa_z = 2\pi/\lambda_z$ is the spwnaise wavenumber. The dashed line in panel (b) marks $\lambda_z = 2L_{\text{sep}}$.

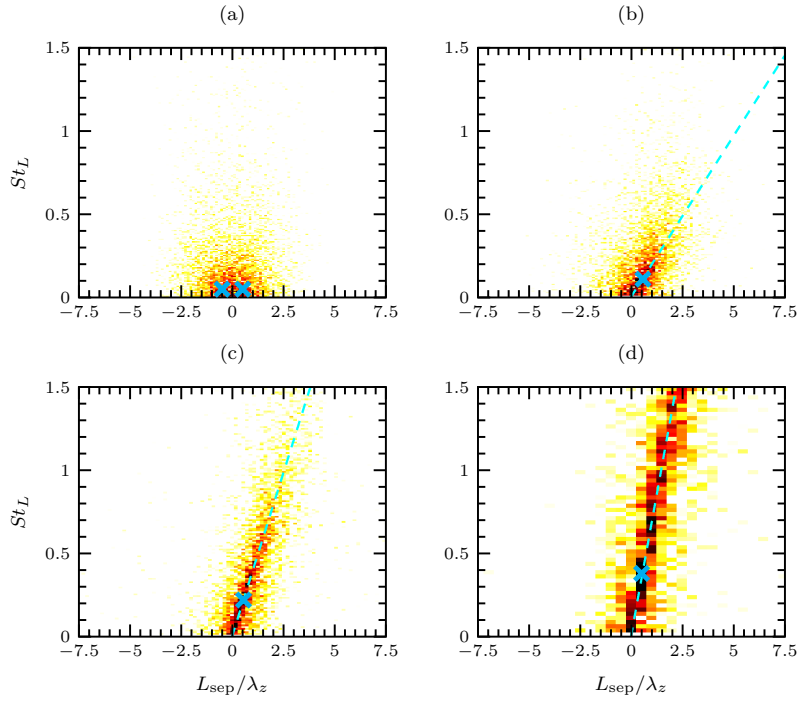

Figure 1.14: Contour plots of transverse wavenumber-frequency spectra of wall pressure at the mean separation location. Dashed lines denote the linear relationship $\omega = \kappa_z w_c$, with convection velocity $w_c = 0.7 u_{0,x} \tan\gamma_0$. (a) $\gamma_0 = 0°$; (b) $\gamma_0 = 15°$; (c) $\gamma_0 = 30°$; (d) $\gamma_0 = 45°$. The white crosses mark the position of the low-frequency peaks.

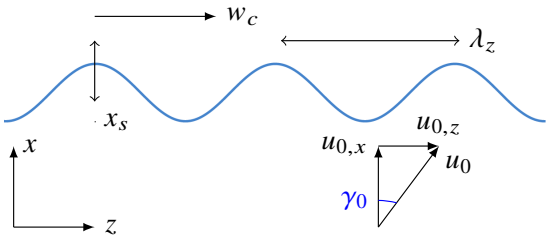

Figure 1.15: Sketch of envisaged oscillation of the separation line.

1.14 to characterize the advection velocity of pressure disturbances. Whereas no clear organization is observed in unswept SBLI (panel (a)), distinct clustering of the PSD around a linear distribution is found in swept interactions, which becomes more evident at high sweep angles, and which is a clear indication of the presence of convecting disturbances. In particular, data fitting yields $\omega = w_c\kappa_z$, with convection velocity proportional to the cross-flow free-stream velocity, namely $w_c \approx 0.7u_{0,z} = 0.7u_{0,x}\tan\gamma_0$.

Based on the above evidence, a tentative model for the behavior of pressure fluctuations near the separation line in swept SBLI is formulated, as sketched in figure 1.15. Specifically, we assume that the separation line oscillates sinusoidally in space with wavelength $\lambda_z = \alpha L_{\text{sep}}$, and in time with frequency f_0, such that $St_{L,0} = f_0 L_{\text{sep}}/u_{0,x}$ is the typical Strouhal number for two-dimensional breathing. Further assuming that pressure disturbances are convected along the z direction at speed $w_c = \eta u_{0,x}\tan\gamma_0$, the behavior of pressure fluctuations along the shock-foot can be described as

$$p'(z,t) \sim e^{\pm i2\pi f_0 t}\, e^{\pm i2\pi(z-w_c t)/\lambda_z} = e^{\pm i2\pi z/\lambda_z}\, e^{i2\pi t(\pm f_0 \mp w_c/\lambda_z)}\,,$$

which implies that the typical nondimensional frequency of oscillation in swept SBLIs is

$$St_L = \left| St_{L,0} \pm \frac{\eta\,\tan\gamma_0}{\alpha} \right|\,, \tag{1.17}$$

with $\alpha \approx 2$ and $\eta \approx 0.7$ as obtained from the previous analysis, and $St_{L,0} \approx 0.04$.

Figure 1.16(a) shows the pre-multiplied pressure PSD at the separation line for fixed shock strength and increasing sweep angle. All distributions exhibit a bump at the high-frequency end, which is associated with the boundary layer turbulence dynamics. In addition, they show prominent peaks at much lower frequency, which however are shifted to the right and increase in magnitude as the sweep angle grows. The model in equation (1.17) predicts two distinct frequencies, but one should regard those as broadband peaks that could well merge into one if sufficiently wide. Quantitative comparison of the numerically computed peak frequencies with the prediction of equation (1.17) is presented in figure 1.16(b), in which we also include results of DNS with different shock strength. The prediction is clearly quite good, perhaps with exception of the single data point corresponding to $\gamma_0 = 30°$, $\theta = 8°$, which features a relatively small separation bubble. Overall, we find that the agreement becomes more satisfactory as the sweep angle increases, which is consistent with stronger coherence of convecting pressure disturbances noticed when discussing figure 1.14.

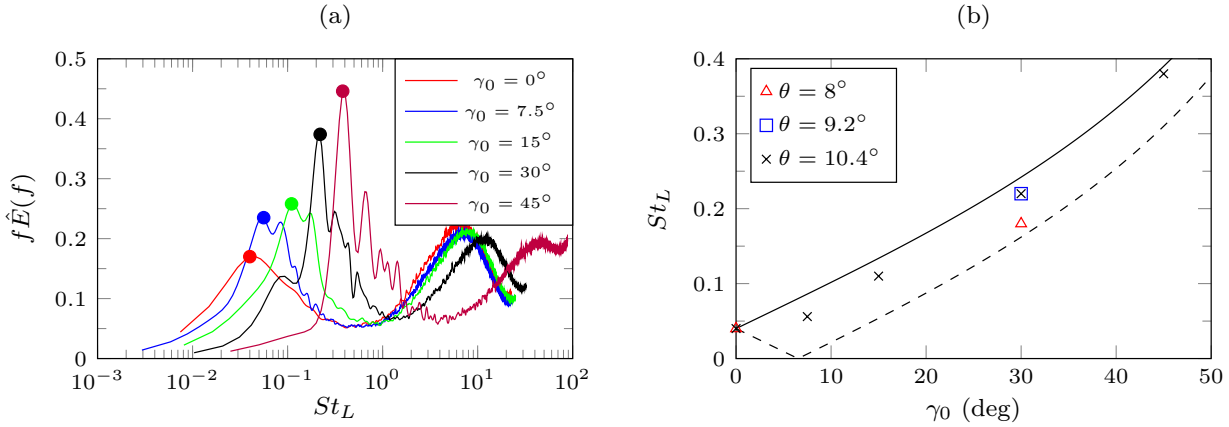

Figure 1.16: (a) Pre-multiplied, normalized frequency spectra of wall pressure at mean separation line for various sweep angles and for fixed shock strength ($\theta = 10.4°$). Peaks are marked with bullets. (b) Peak frequency as a function of sweep angle: the solid and dashed lines denote the prediction of equation (1.17)

3.2 Inflow conditions for high-speed turbulent boundary layers

As explained in previous sections, the numerical investigation on inflow effects comprises two different sets of simulations. Benchmark results are briefly outlined in the following section, followed by the analysis of the short-domain computations for the assessment of inflow conditions.

Results of benchmark simulations

Benchmark cases are used to extract high-fidelity laws for one or several diagnostic parameters, which allow to ascertain that an equilibrium turbulence state is achieved. The first diagnostic implies fulfillment of mean momentum balance (Smits & Dussauge, 2006). Mean momentum balance, if integrated in wall-normal direction, combined with the continuity equation and the assumption of zero external pressure gradient, leads to the compressible equivalent of the von Kármán equation, originally derived for incompressible flow (Ross, 1953),

$$\frac{C_f}{2} = \frac{\mathrm{d}\theta}{\mathrm{d}x} + \frac{1}{\rho_0 u_0^2}\frac{\mathrm{d}}{\mathrm{d}x}\int_0^\delta \bar{\rho}(\widetilde{v''v''} - \widetilde{u''u''})\mathrm{d}y, \tag{1.18}$$

where

$$\theta = \int_0^\delta \frac{\bar{\rho}\tilde{u}}{\rho_0 u_0}\left(1 - \frac{\tilde{u}}{u_0}\right)\mathrm{d}y,$$

is the momentum boundary layer thickness. Equation (1.18) also includes a term depending on the streamwise variation of the turbulent stresses, which may be relevant at high Mach number (Finley, 1977). It can be assumed that an equilibrium state is reached if the residual of equation (1.18) is smaller than a certain prescribed tolerance (Schlatter *et al.*, 2010*b*; Wenzel

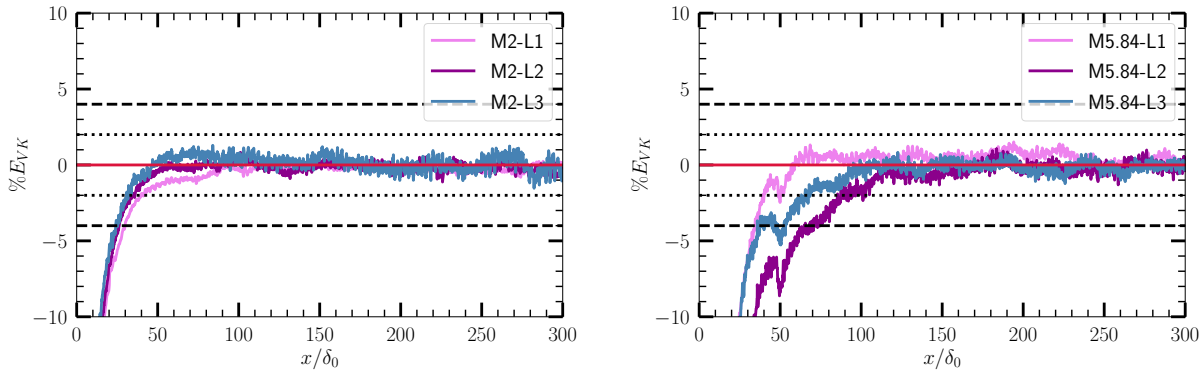

Figure 1.17: Supersonic (left) and hypersonic (right) boundary layer benchmark flow cases: streamwise distributions of relative error in mean momentum balance. Solid lines denote the DNS data, dashed lines denote a ±4% error band, and dotted lines denote a ±2% error band.

et al., 2018; Huang *et al.*, 2022). We thus define a relative error in this metric as

$$E_{\mathrm{VK}} = \frac{C_f/2 - \mathrm{d}\hat{\theta}/\mathrm{d}x}{C_f/2}, \tag{1.19}$$

where

$$\hat{\theta} = \theta + \frac{1}{\rho_0 u_0^2}\int_0^\delta \bar{\rho}(\widetilde{v''v''} - \widetilde{u''u''})\mathrm{d}y.$$

Figure 1.17 shows the distribution of the relative error in mean momentum balance, as defined in equation (1.19), for supersonic and hypersonic benchmark simulations in long domains. Large errors are found close to the inflow, similar to what reported by Schlatter *et al.* (2010*b*) for incompressible boundary layers. The hypersonic benchmark flow cases require longer inflow length as compared to the supersonic cases. In fact, about $35 - 70\delta_0$ are needed in order to fall within the 4% accuracy band in hypersonic cases, in contrast with the $\approx 20\delta_0$ required for the supersonic benchmark. This finding is consistent with previous results of Wenzel *et al.* (2018) and Huang *et al.* (2022), who reported monotonic increase of the inflow length with the free-stream Mach number. We additionally find that DNS with higher inflow Reynolds number require longer distance to adjust. Momentum balance is generally satisfied to within 1% error only at a distance of about $100 - 150\delta_0$. For further safety margin, we only consider the last third part of the domain to develop reference correlation laws for the various diagnostic quantities.

Two additional metrics refer to the development of the peaks of the turbulent shear stress, $\tau_{xy}^{\mathrm{pk}} = \max_y(-\bar{\rho}\widetilde{u''v''}/\tau_w)$, and of the streamwise velocity variance, $\tau_{xx}^{\mathrm{pk}} = \max_y(\bar{\rho}\widetilde{u''u''}/\tau_w)$. Correlations for the peak turbulent shear stress were suggested by Chen *et al.* (2019)

$$\tau_{xy}^{\mathrm{pk}} = 1 - B_1 \mathrm{Re}_\tau^{-6/7}, \tag{1.20}$$

with $B_1 = 13.7$ for incompressible flow. As regards the streamwise velocity variance, Pirozzoli & Bernardini (2013) found it grows logarithmically with Re_τ,

$$\tau_{xx}^{\mathrm{pk}} = A_2 + B_2 \log \mathrm{Re}_\tau, \tag{1.21}$$

Fit coefficients	Supersonic benchmark	Hypersonic benchmark
B_1	13.62	29.8
A_2, B_2	3.35, 0.725	-
A_3, B_3	0.0174, 0.245	0.0131, 0.268
A_4, B_4	-7.09, 2.23	3.37, 1.32
A_5, B_5	-	0.00774, 0.272

Table 1.4: List of fitting coefficients in equations (1.20)-(1.24), as derived from supersonic and hypersonic benchmark DNS.

with $A_2 = 3.35$ and $B_2 = 0.725$. Two obvious additional diagnostic parameters include the friction coefficient (C_f) and the heat transfer coefficient,

$$C_h = \frac{q_w}{\rho_0 u_0 C_p (T_w - T_r)} \tag{1.22}$$

where $q_w = k\partial T/\partial y|_w$ is the wall heat flux, with $k = \mu/(Pr\, C_p)$ the thermal conductivity. Power-law relationships versus Re_θ are generally assumed for these parameters, namely

$$C_f = A_3 \mathrm{Re}_\theta^{-B_3}, \quad C_h = A_5 \mathrm{Re}_\theta^{-B_5}, \tag{1.23}$$

where $A_3 = 0.024$, $B_3 = 0.25$ for incompressible flow (Smits *et al.*, 1983). Finally, we consider the wall pressure variance, which is relevant in aero-vibroacoustic analysis. As shown by Jiménez *et al.* (2010) and Pirozzoli & Bernardini (2011), this quantity also includes contributions from distant eddies residing in the outer layer, hence incomplete boundary layer development may reflect into inaccurate prediction of this indicator. Farabee & Casarella (1991) found a convenient representation in the form,

$$\overline{p_w'^2}^+ = A_4 + B_4 \log \mathrm{Re}_\tau, \tag{1.24}$$

with $A_4 = -4.30$, $B_4 = 1.86$ for incompressible flow.

The 'long' DNS are found to conform very well with the present set of correlation laws, if all fitting coefficients are properly derived in each condition. Streamwise trends of the friction coefficient, wall heat transfer coefficient, Reynolds stress peaks and pressure variance are omitted for the sake of brevity. The results of the benchmark cases are briefly summarized in Tab. 1.4 in terms of their fitting coefficients, both for the supersonic and hypersonic cases.

Effect of inflow turbulence seeding – supersonic flow cases

Data from DNS in short domains are shown here, with the goal of evaluating the influence of the inflow seeding technique on the establishment of an equilibrium turbulence state, using the correlations established in the previous paragraphs as a benchmark.

Figure 1.18 shows the distribution of the relative error in von Kármán equation for supersonic flow cases in relatively short domains. All DNS fall inside the 4% error band past at a distance 10-25δ_0 from the inflow. Past this point, some scatter across curves is found, with

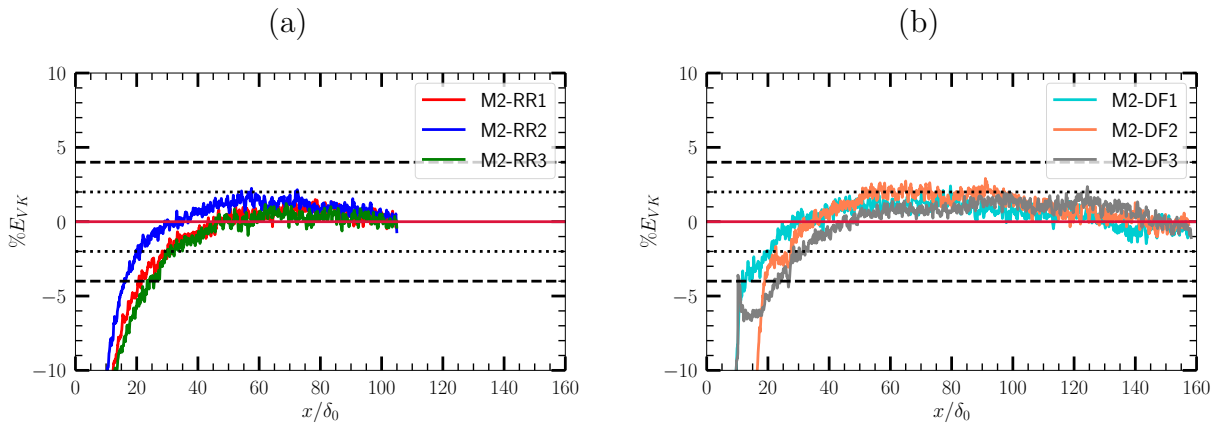

Figure 1.18: Supersonic flow cases: streamwise distributions of relative error in mean momentum balance. The solid lines denote DNS data using RR inflow (a) and DF inflow (b); the dashed and the dotted lines denote ±4% and ±2% error bands, respectively.

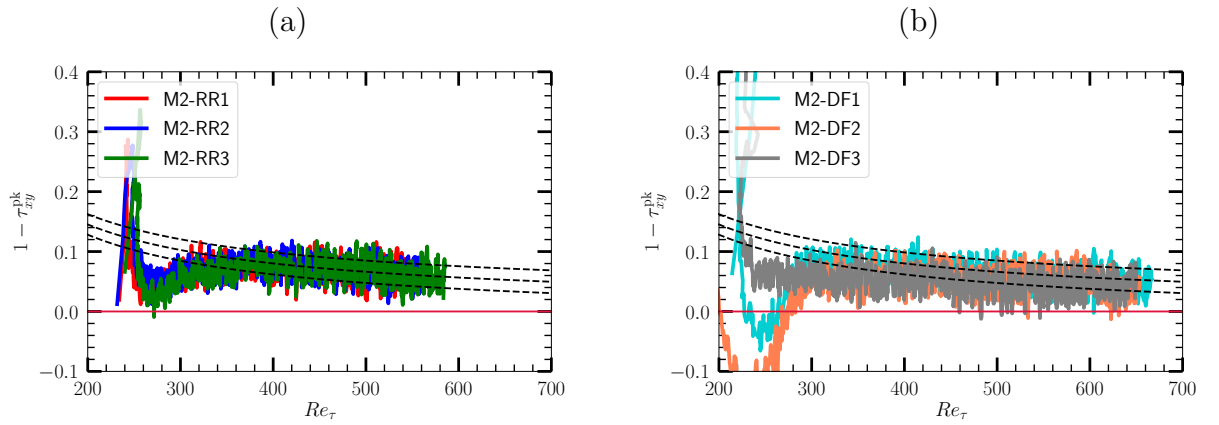

Figure 1.19: Supersonic flow cases: distributions of peak turbulent shear stress as a function of friction Reynolds number. The solid lines denote DNS data using RR inflow (a) and DF inflow (b); the dashed lines denote depict reference distributions obtained from the benchmark DNS and a ±2% error band.

RR generally performing better than DF, in that it yields smaller error for given distance from the inflow. No systematic differences are observed among different implementations of the two techniques. Figure 1.19 shows the distributions of the peak turbulent shear stress, which highlights some differences among the various approaches. Whereas the shear stress peak never exceeds unity in all DNS with RR, the DF1 and the DF2 cases exceed this threshold in a large region near the inflow, which makes the flow statistics quite unphysical. On the other hand, the DF3 implementation yields results more similar to RR, and quicker adjustment to equilibrium. The peak shear stress appears to monotonically approach unity at $\mathrm{Re}_\tau \approx 400$, but careful inspection of the figure suggests that DF tends to overestimate the trends returned from the benchmark DNS (dashed line), and to occasionally exceed unity. The peak streamwise velocity variance is shown in figure 1.20. Notably, the DF has a more benign behavior

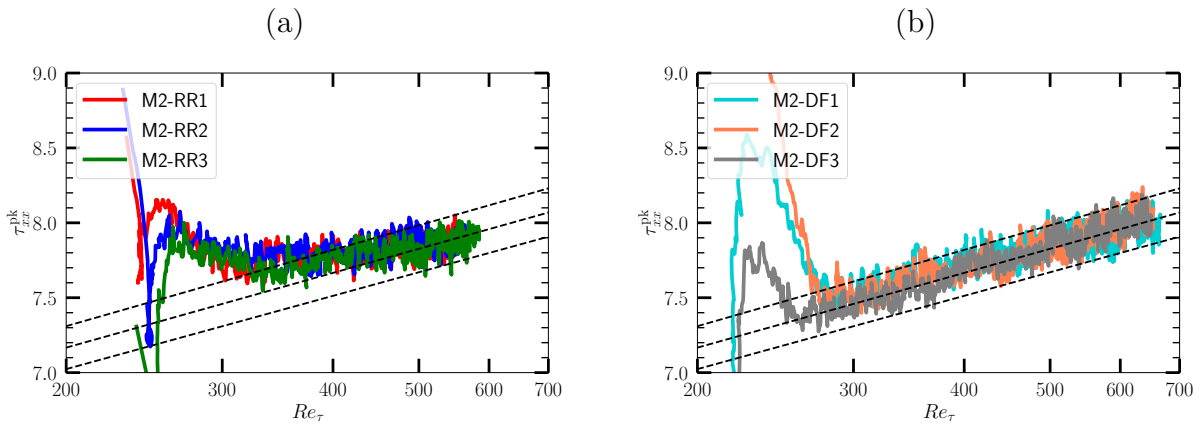

Figure 1.20: Supersonic flow cases: distributions of peak streamwise turbulent stress as a function of friction Reynolds number. The solid lines denote DNS data using RR inflow (a) and DF inflow (b); the dashed lines denote reference distributions obtained from the benchmark DNS, and a ±2% error band.

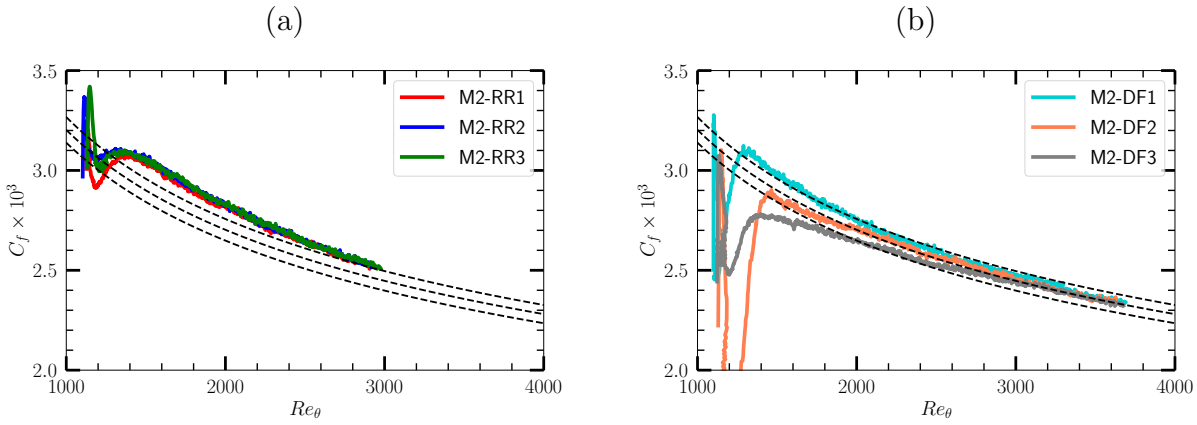

Figure 1.21: Supersonic flow cases: distributions of friction coefficient as a function of momentum thickness Reynolds number. The solid lines denote DNS data using RR inflow (a) and DF inflow (b); the dashed lines denote reference distributions obtained from the benchmark DNS, and a ±2% error band.

regarding this variable, as all DF implementations attain the correct behaviour at $\mathrm{Re}_\tau \gtrsim 300$, despite large excursions from the reference trends in the initial transient. On the other hand, values in excess of $\mathrm{Re}_\tau = 400$ are needed for RR statistics to fall within the ±2% error band. As a result, RR requires longer fetch ($x/\delta_0 \approx 80$) for proper development of the streamwise turbulent stress. The DF technique also appears to perform better than RR as regards the prediction of the friction coefficient, as shown in figure 1.21. In fact, despite much smoother initial transient, RR tends to consistently overpredict C_f, with values falling within ±2% error only at $\mathrm{Re}_\theta \gtrsim 3000$, corresponding to the end of the computational domain employed for these DNS. The results of all RR-based DNS are quite similar, meaning that implementation details are unimportant in the observed behavior. Despite substantial differences in the inflow

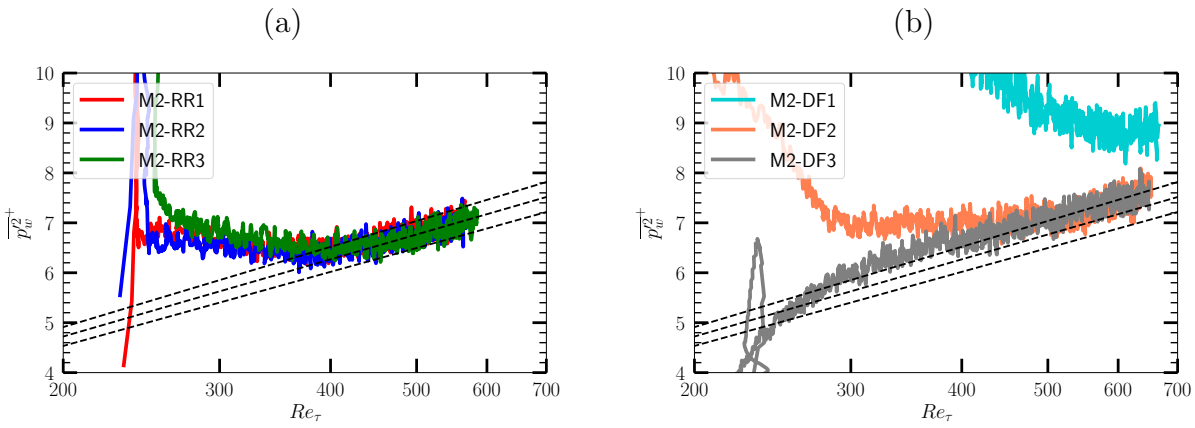

Figure 1.22: Supersonic flow cases: distributions of wall pressure variance as a function of friction Reynolds number. Solid lines denote DNS data using RR inflow (a) and DF inflow (b); the dashed lines denote reference distributions obtained from the benchmark DNS, and a ±4% error band.

recovery region, all DF implementations yield a C_f within a ±2% error band at $\mathrm{Re}_\theta \gtrsim 2000$, i.e. at $x/\delta_0 \gtrsim 50$, and basically landing on the benchmark distribution at $\mathrm{Re}_\theta \approx 3000$. The DF3 implementation seems to be a bit slower than the other in this respect. It is noteworthy that the strong dips next to the inflow section seen in the DF simulations could in principle be mitigated as suggested by Larsson (2021).

The von Kármán equation (1.18) can be used to connect observations made regarding the friction coefficient and the peak streamwise turbulent stress. In fact, figure 1.18 highlights irregular distribution of C_f next to the inflow in the DF simulations, with sharp increase, followed by abrupt drop. The von Kármán equation clarifies that those regions are connected with u' fluctuations, as the initial increase in the momentum flux deficit (namely $\mathrm{d}\theta/\mathrm{d}x$) and decrease of wall shear stress compensate the growth of the streamwise stress. This mechanism is reversed in the ensuing region, featuring strong reduction of the streamwise stress an growth of the wall shear stress.

The distributions of the wall pressure variance are shown in figure 1.22. All RR implementations exhibit roughly similar behaviour, as they achieve a monotonically increasing trend compatible with theory (Farabee & Casarella, 1991; Pirozzoli & Bernardini, 2011) and with the benchmark distribution at $\mathrm{Re}_\tau \gtrsim 450$ (namely $x/\delta_0 \gtrsim 60$). The behaviour of the DF-based DNS is richer as different trends are found depending on the implementation details. In fact, the baseline DF1 implementation largely overpredicts pressure fluctuations, throughout the computational domain. This large disagreement is partially cured through suppression of the streamwise velocity fluctuations in the DF2 implementation, and even more by making the inflow cross-stream velocity divergence-free, as in the DF3 implementation. Both DF2 and DF3 indeed exhibit reasonably correct trends at $\mathrm{Re}_\tau \gtrsim 300$ and $\mathrm{Re}_\tau \gtrsim 400$, respectively, which is in line if not better than for the RR cases. Still, some consistent overprediction of pressure disturbances in the developed region is observable, which we interpret as the result of acoustic disturbances arising at the inlet owing to the unrealistic structure of the inflow velocity fluctuations.

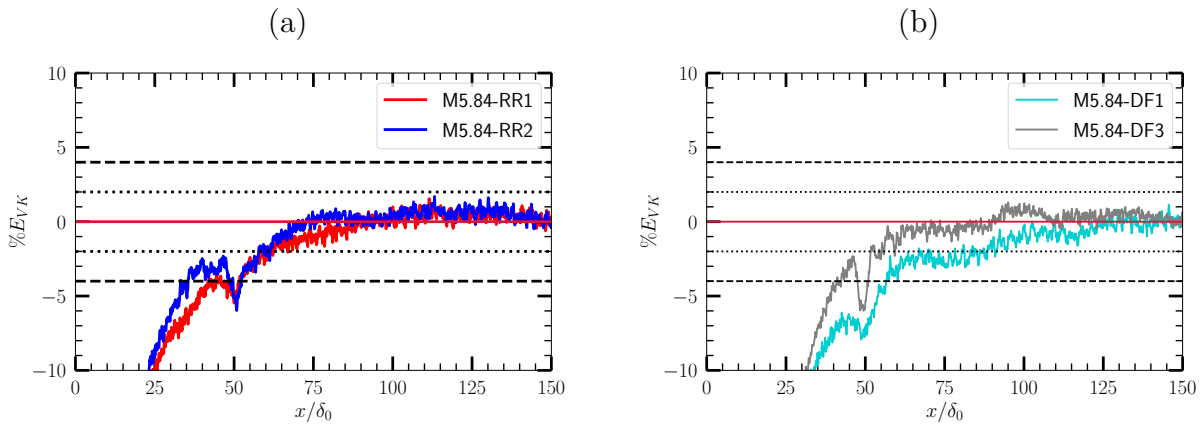

Figure 1.23: Hypersonic flow cases: streamwise distributions of error in mean momentum balance. The solid lines denote DNS data using RR inflow (a) and DF inflow (b); the dashed and dotted lines denote a ±4% and ±2% error band, respectively.

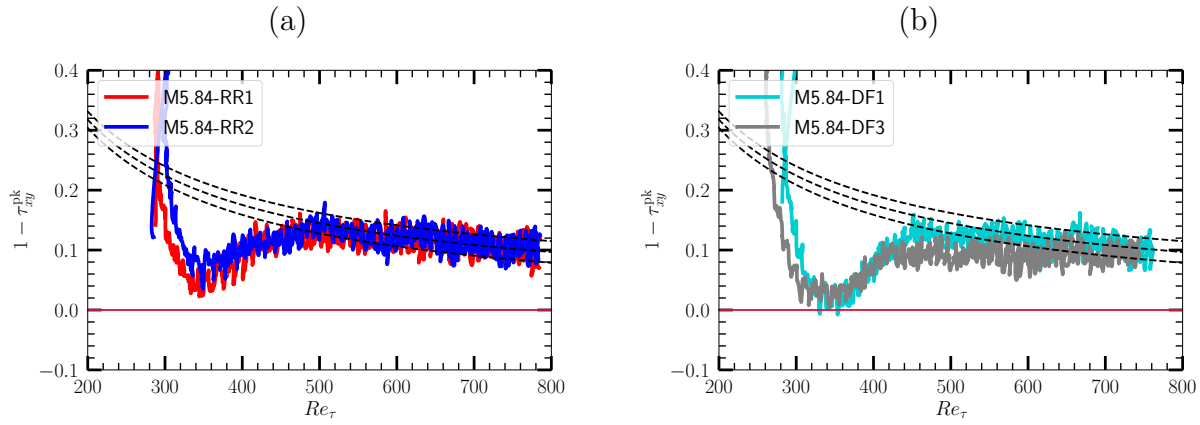

Figure 1.24: Hypersonic flow cases: distributions of peak turbulent shear stress as a function of friction Reynolds number. The solid lines denote DNS data using RR inflow (a) and DF inflow (b); the dashed lines denote depict reference distributions obtained from the benchmark DNS and a ±2% error band.

Effect of inflow turbulent seeding – hypersonic flow cases

Figure 1.23 shows the relative error for the von Kármán equilibrium condition for the RR (left panel) and DF (right panel) techniques. The two RR implementations herein considered have quite similar behaviour, with ±4% error band attained at $x \gtrsim 50\delta_0$, and the stricter threshold ±2% is reached at $x \gtrsim 60\delta_0$. Regarding DF cases, the baseline DF1 implementation is slower to adjust towards zero error, whereas the DF3 implementation (suppression of u' and streamfunction formulation) readjusts more quickly, falling within the ±2% error band quite early ($x \gtrsim 50\delta_0$). The peak turbulent shear stress is shown in Figure 1.24, as a function of the friction Reynolds number. Unlike the supersonic cases, the peaks for both RR and DF cases remain strictly below unity, throughout the computational domain. Near equilibrium

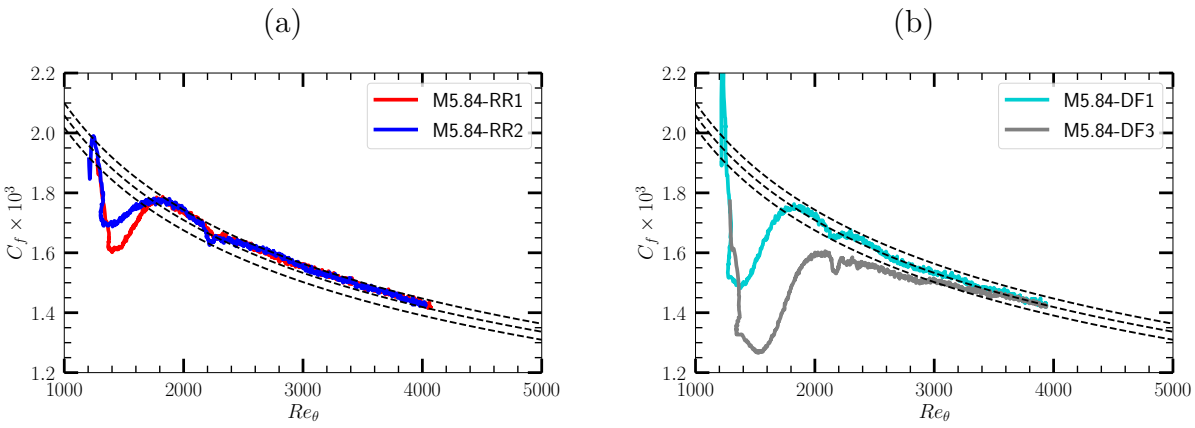

Figure 1.25: Hypersonic flow cases: distributions of friction coefficient as a function of momentum thickness Reynolds number. The solid lines denote DNS data using RR inflow (a) and DF inflow (b); the dashed lines denote reference distributions obtained from the benchmark DNS, and a ±2% error band.

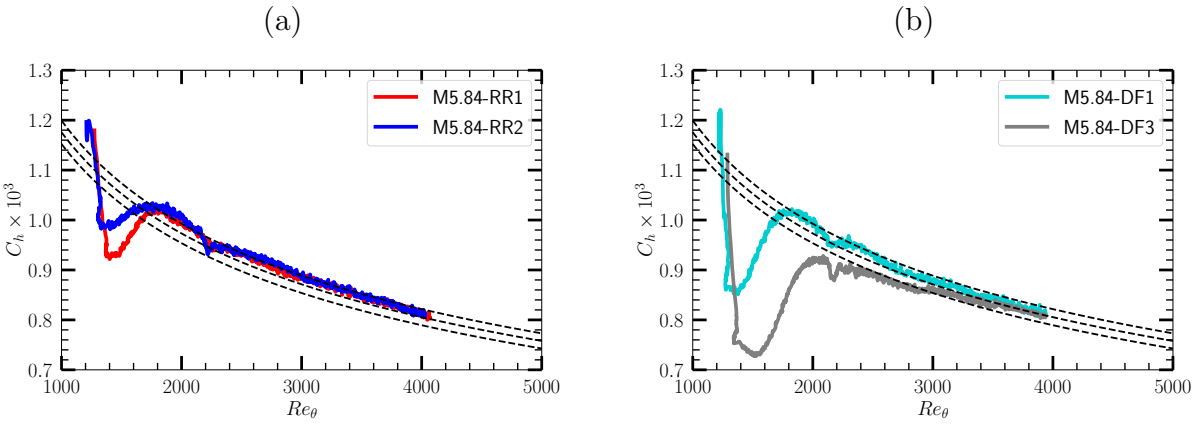

Figure 1.26: Hypersonic flow cases: distributions of heat transfer coefficient as a function of momentum thickness Reynolds number. The solid lines denote DNS data using RR inflow (a) and DF inflow (b); the dashed lines denote reference distributions obtained from the benchmark DNS, and a ±2% error band.

conditions are reached for $\mathrm{Re}_\tau \gtrsim 500$ (corresponding to $x \approx 55\delta_0$ for RR1, RR2, DF1 and $x \approx 75\delta_0$ for DF3). At higher Re the RR cases consistently follow the benchmark correlation, as the DF1 case also does. On the other hand the DF3 method seems to exhibit a plateau, followed by decline at $\mathrm{Re}_\tau \gtrsim 600$ (corresponding to $x \approx 100\delta_0$). Figures 1.25 and 1.26 show the distributions of the friction coefficient and the heat transfer coefficient as a function of the momentum thickness Reynolds number. Not surprisingly, the two quantities exhibit a similar behavior. We find that RR inflow feeding yields results which, past an initial dip, fall quite rapidly within the ±2% error band. The dip is found to be much larger when DF is used. However, as also found for the shear stress, the baseline DF1 implementation adjusts quite quickly at $\mathrm{Re}_\theta \approx 2000$ similar to the RR cases, whereas the DF3 implementation requires

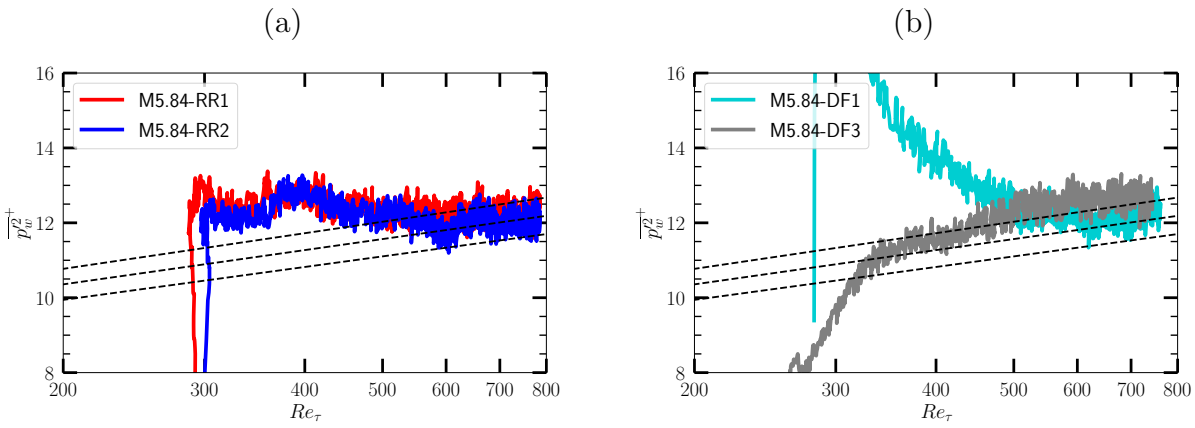

Figure 1.27: Hypersonic flow cases: distributions of wall pressure variance as a function of friction Reynolds number. Solid lines denote DNS data using RR inflow (a) and DF inflow (b); the dashed lines denote reference distributions obtained from the benchmark DNS, and a ±4% error band.

longer fetch to reach equilibrium, at $\mathrm{Re}_\theta \gtrsim 3000$ (corresponding to $x \gtrsim 95\delta_0$). In figure 1.27 we finally consider the wall pressure variance. Regarding this parameter, the RR method is capable of attaining a monotonically increasing trend with the Reynolds number at $\mathrm{Re}_\tau \gtrsim 600$ (corresponding to $x \gtrsim 80\delta_0$), hence the inflow adjustment length is much more than for supersonic cases. Past that location the data are in fair agreement with the benchmark correlation. The DF seeding exhibits results similar to the supersonic case. Whereas the baseline DF1 implementation starts from very large values and it tends to adjust to the expected behavior towards the end of the computational domain, the use of solenoidal inflow fluctuations in the DF3 implementation yields a realistic behavior starting much closer to the inflow ($\mathrm{Re}_\tau \gtrsim 350$, corresponding to $x \gtrsim 30\delta_0$). In any case, pressure fluctuations in the developed region appear to be a bit larger than expected, thus corroborating the notion that the DF technique is inherently more noisy than RR.

Concluding remarks

We next attempt to draw a quantitative comparison of the predictive capabilities of the various inflow turbulence seeding techniques in terms of achieving accurate representation of a state of fully developed turbulence. For that purpose, in figures 1.28 and 1.29 we show, for each diagnostic parameter herein identified, the inflow distance needed to target the benchmark correlations previously determined to a given accuracy. For the sake of the present analysis, the flow statistics shown in the previous sections have been smoothed by using a Savitzky–Golay causal filter.

Inspecting the results of supersonic DNS in figure 1.28, one may infer that DF seeding is capable of achieving faster adaptation of the friction coefficient than RR. In fact, all DF implementations achieve ±2% confidence within $80\delta_0$ from the inflow, with DF2 substantially faster, with inflow length of about $30\delta_0$. RR feeding does not seem to reach the same level of accuracy within the selected computational domain, the error on friction being still 2%

error at $100\delta_0$. The same error is obtained by all RR implementations, which also exhibit very similar trends. Regarding the peak streamwise velocity variance stress, one can likewise conclude that the DF1 and DF3 implementations are marginally better than RR. The DF2 case is obviously disadvantaged in this respect, as it has the lowest inflow turbulence kinetic energy. This criterion is however not very restrictive, as all RR and DF simulations require at most $40\delta_0$ to achieve $\pm 2\%$ accuracy. The wall pressure variance exhibits quite a different behavior. In fact, whereas RR shows consistent convergence towards the reference equilibrium value, DF in its variants consistently overpredict this property. Improvements over baseline DF1 are obtained from formulations DF2 and DF3, which nevertheless require an inflow length of about $100\delta_0$ to achieve 5% accuracy. Proposed variants of the RR technique (mainly the RR2 implementation) yield small but observable improvement in this metric as may be argued upon close inspection of figure 1.22 (a). Reducing the intensity of streamwise turbulent fluctuation intensity of DF thus yields beneficial effects on the wall pressure variance, but on the other hand it yields poorer prediction of the peak shear stress. As a result, at least $60\delta_0$ are required to achieve 3% error in this quantity, whereas DF1 and all RR implementations require $30\delta_0$ for 2% tolerance. Baseline DF1 however outperforms alternative implementations regarding the prediction of the peak shear stress, offering similar performance as RR in this respect.

These conclusions need some adaptation for the hypersonic flow cases (see figure 1.29). In particular, we find that this time the baseline DF inflow feeding, while retaining minor advantage over baseline RR in the prediction of the friction and heat transfer coefficients, also yields similar predictions of the wall pressure variance and of the peak turbulent shear stress. Regarding the proposed modifications, we find that the RR2 implementation yields some advantage in making RR less noisy, while worsening the prediction of C_h a bit. The beneficial effects of removing the streamwise velocity fluctuations in the DF3 implementation are instead lost, and instead we find significant deterioration in the prediction of friction and wall pressure variance. This is the likely a result of very slow transition of the flow to a fully turbulent state, as suggested by figure 1.25 (b).

Additional insight into the tendency of the flow statistics towards equilibrium can be gained by expressing the streamwise fetch from the inflow in terms of eddy-turnover times, by exploiting Taylor's hypothesis (Simens *et al.*, 2009) to define

$$\mathrm{ETT} = \frac{x/u_0}{\delta_0/u_\tau} = \frac{x}{\delta_0}\sqrt{\frac{C_f}{2}}. \tag{1.25}$$

This is done for the error in the mean momentum balance in figure 1.30 (a-b), which highlights that all simulations collapse after four ETT, regardless of the inflow seeding. All supersonic cases fall within $\pm 4\%$ error band after about one ETT, while the hypersonic cases after 1.5-2 ETT, in agreement with literature results (Huang *et al.*, 2022). Regarding the friction coefficient, figure 1.30 (c-d), shows that, whereas different inflow seeding yields different degree of accuracy in the initial transient, convergence to the benchmark distribution is basically complete after seven eddy turnover times for supersonic cases, and after about four turnover times in hypersonic cases, regardless of the seeding and of the inflow Reynolds number. As noted previously, the DF2 seeding yields faster adjustment of this particular parameter in the supersonic flow case, whereas baseline RR and DF seem to be most effective in the hypersonic flow case.

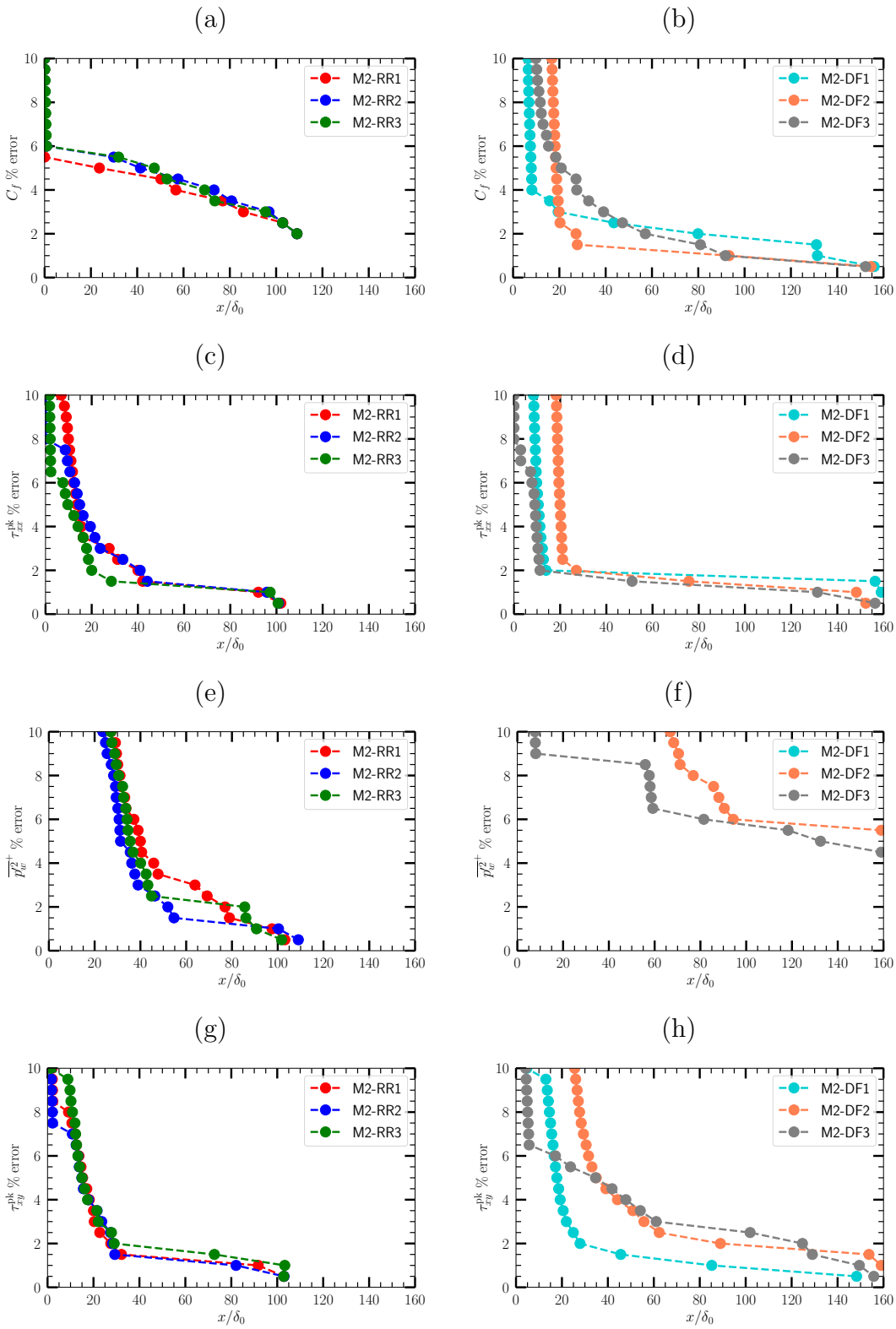

Figure 1.28: Inflow length for supersonic flow cases as function of target percent error with respect to benchmark DNS for diagnostic quantities under scrutiny: (a, b) friction coefficient, (c, d) peak streamwise velocity variance, (e, f) wall pressure variance, and (g, h) peak turbulent shear stress. Left column RR, right column DF.

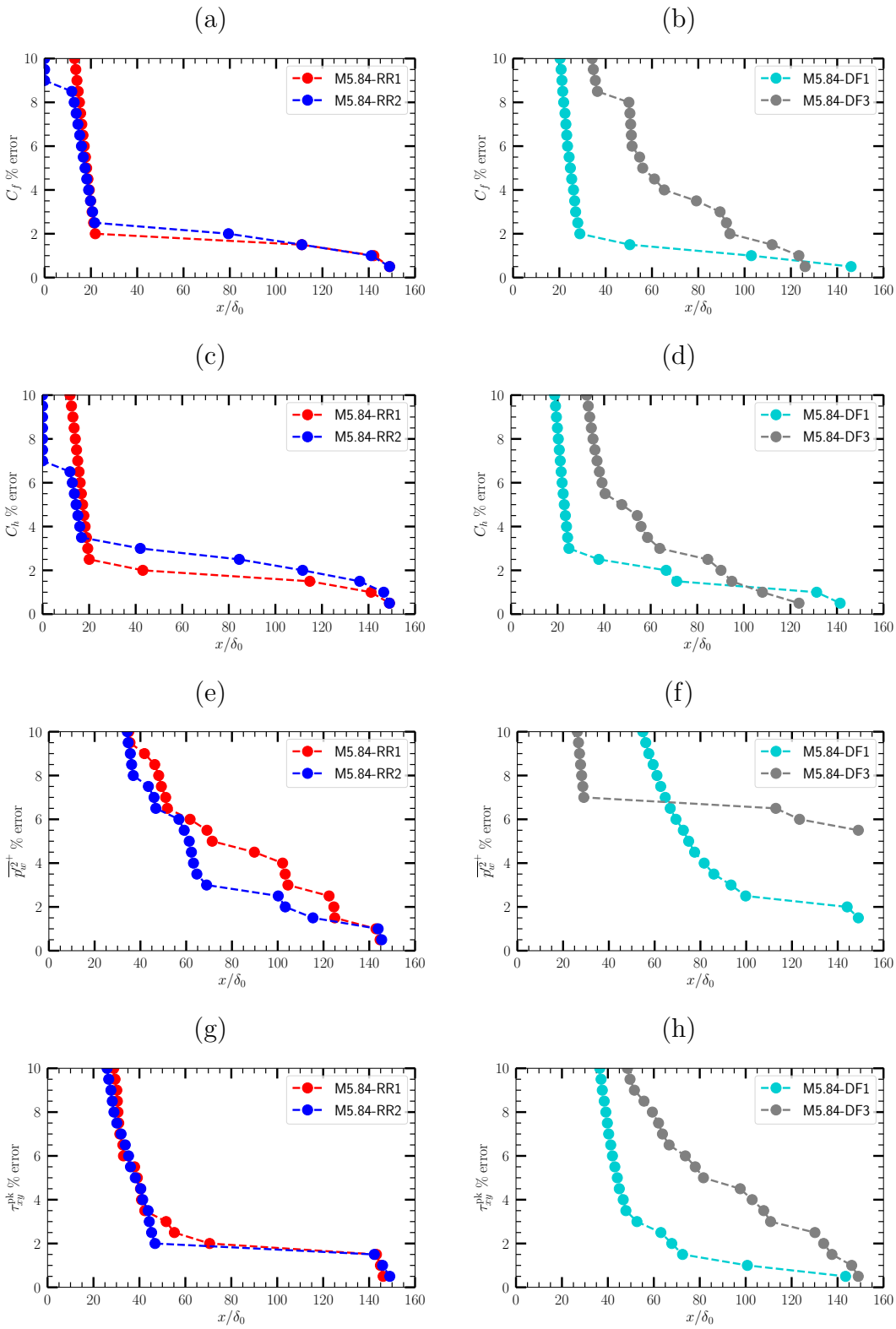

Figure 1.29: Inflow length for hypersonic flow cases as function of target percent error with respect to benchmark DNS for diagnostic quantities under scrutiny: (a, b) friction coefficient, (c, d) heat transfer coefficient, (e, f) wall pressure variance, and (g, h) peak turbulent shear stress. Left column RR, right column DF.

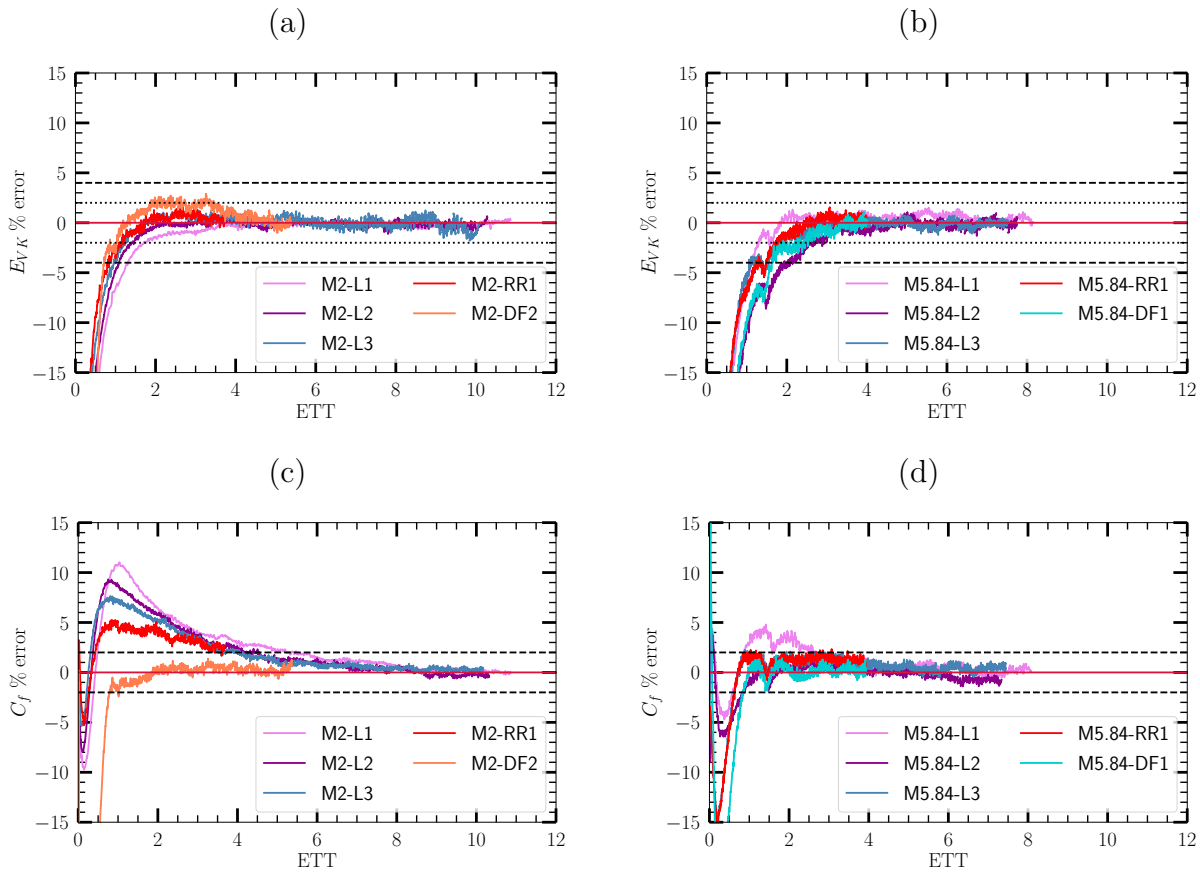

Figure 1.30: Error in mean momentum balance (a,b) and in friction coefficient (c,d), as a function of number of eddy-turnover times ETT for supersonic (a,c) and hypersonic (b,d) flow cases. The solid lines denote DNS data. The dashed lines in (c,d) denote ±4% error bands and the dotted lines ±2% error bands. The dashed lines in (a,b) denote ±2% error bands.

4. Conclusions

The present report describes two research activities carried out by the research group in the context of high-fidelity simulations of the three-dimensional interaction between a shock and a boundary layer. The main research line is devoted to the numerical simulation of the interaction between an oblique shock wave and a supersonic/hypersonic turbulent boundary layer in presence of a crossflow. A simplified configuration, denoted SSBLI in the present work, is used to isolate the effect of the crossflow on the interaction. The analysis of the mean flow properties reveals that the recirculation region is larger for the skewed cases, and its streamwise length increases non-linearly with the sweep angle. Strong flow non-equilibrium is detected past reattachment, especially for the supersonic case. The flow direction is clearly different from the inviscid distribution, and severe misalignment between the Reynolds stresses and the flow mean strain is found, meaning that standard Reynolds-averaged turbulence models could fail in accurately predicting this kind of flow. The study of low frequency unsteadiness in wide domains reports increase of the peak frequency of pressure spectra at separation line with sweep angle. Proper Orthogonal Decomposition of instantaneous wall pressure fields links these pressure oscillations with large scale rippling at separation line; subsequent analysis allows estimation of the typical rippling velocity and length scales as a function of the skew angle.

A parallel research line focused on the effect of the inflow conditions on the numerical simulations of spatially-developing turbulent boundary layers. This subject is widely debated within the fluid-dynamic research community as it involves the reliability of numerical dataset for the prediction of quantities of engineering interest as heat transfer rates and skin friction. Two sets of numerical simulations are carried out: 'long' computations are used to generate reference scaling laws, which are devoid of inflow effects, for quantities of interest as wall friction, heat transfer, wall pressure and turbulent stress peaks. Simulations on short domains (whose dimensions match the one typically used in previous literature studies) are used to assess the effect of inflow conditions on the spatial development of the flow. It is found that, depending on the flow conditions and the inflow strategies, a certain distance ('inflow length') is required for each quantity to match the reference laws. Whereas the supersonic case reveals that standard DF methods have unrealistically large wall pressure variance, they also appear to yield superior performance in predicting skin friction and streamwise Reynolds stress. Modifications to DF method are proposed, which successfully solve the wall pressure variance issue. On the other hand, similar behaviour of standard RR and DF inflow procedure is found for the hypersonic case, hence no advantage can be gained in using the modified DF approach in this flow regime.

References

Adler, M. C. & Gaitonde, D. V. 2018 Dynamic linear response of a shock/turbulent-boundary-layer interaction using constrained perturbations. *Journal of Fluid Mechanics* **840**, 291–341.

Adler, M. C. & Gaitonde, D. V. 2019 Flow similarity in strong swept-shock/ turbulent-boundary-layer interactions. *AIAA Journal* **57** (4), 1579–1593.

Adler, M. C. & Gaitonde, D. V. 2020 Dynamics of strong swept-shock/turbulent-boundary-layer interactions. *Journal of Fluid Mechanics* **896**, A29.

Adler, M. C., Gonzalez, D. R., Stack, C. M. & Gaitonde, D. V. 2018 Synthetic generation of equilibrium boundary layer turbulence from modeled statistics. *Computers & Fluids* **165**, 127–143.

Arora, N., Mears, L. & Alvi, F. 2019 Unsteady characteristics of a swept-shock/boundary-layer interaction at Mach 2. *AIAA J.* **57**, 4548–4559.

Babinsky, H. & Harvey, J. K. 2011 *Shock wave-boundary-layer interactions*. Cambridge University Press.

Bernardini, M., Modesti, D., Salvadore, F. & Pirozzoli, S. 2021 Streams: A high-fidelity accelerated solver for direct numerical simulation of compressible turbulent flows. *Computer Physics Communications* **263**, 107906.

Ceci, A., Palumbo, A., Larsson, J. & Pirozzoli, S. 2022*a* Numerical tripping of high-speed turbulent boundary layers. *Theoret. Comput. Fluid Dyn.* pp. 1–22.

Ceci, A., Palumbo, A., Larsson, J. & Pirozzoli, S. 2022*b* On low-frequency unsteadiness in swept shock wave / boundary layer interactions, under review. *J. Fluid Mech.* .

Ceci, A. & Pirozzoli, S. 2022 Natural grid stretching for dns of compressible wall-bounded flows, submitted. *J. Comput. Phys.* .

Chen, X., Hussain, F. & She, Z.-S. 2019 Non-universal scaling transition of momentum cascade in wall turbulence. *Journal of Fluid Mechanics* **871**.

Clemens, N. & Narayanaswamy, V. 2014 Low-frequency unsteadiness of shock wave/turbulent boundary layer interactions. *Annu. Rev. Fluid Mech.* **46**, 469–492.

Coleman, G. N., Rumsey, C. L. & Spalart, P. R. 2019 Numerical study of a turbulent separation bubble with sweep. *Journal of Fluid Mechanics* **880**, 684–706.

Dhamankar, N. S., Blaisdell, G. A. & Lyrintzis, A. S. 2018 Overview of turbulent inflow boundary conditions for large-eddy simulations. *Aiaa Journal* **56** (4), 1317–1334.

Di Renzo, M., Oberoi, N., Larsson, J. & Pirozzoli, S. 2021 Crossflow effects on shock wave/turbulent boundary layer interactions. *Theoretical and Computational Fluid Dynamics* pp. 1–18.

Doehrmann, A., Padmanabhan, S., Threadgill, J. & Little, J. 2018 Effect of sweep on the mean and unsteady structures of impinging shock/boundary layer interactions. In *2018 AIAA Aerospace Sciences Meeting*, *AIAA Paper* 2018-2074.

Dolling, D. S. 2001 Fifty years of shock-wave/boundary-layer interaction research: What next? *AIAA Journal* **39** (8), 1517–1531.

Dussauge, J.-P., Dupont, P. & Debiève, J.-F. 2006 Unsteadiness in shock wave boundary layer interactions with separation. *Aero. Sci. Tech.* **10**, 85–91.

Erengil, M. E. & Dolling, D. S. 1993 Effects of sweepback on unsteady separation in mach 5 compression ramp interactions. *AIAA Journal* **31** (2), 302–311.

Erm, L. P. & Joubert, P. N. 1991 Low-reynolds-number turbulent boundary layers. *Journal of Fluid Mechanics* **230**, 1–44.

Fang, J., Yao, Y., Zheltovodov, A. A. & Lu, L. 2017 Investigation of Three-Dimensional Shock Wave/Turbulent-Boundary-Layer Interaction Initiated by a Single Fin. *AIAA Journal* **55** (2), 509–523.

Farabee, T. M. & Casarella, M. J. 1991 Spectral features of wall pressure fluctuations beneath turbulent boundary layers. *Physics of Fluids A: Fluid Dynamics* **3** (10), 2410–2420.

Finley, P. 1977 Static pressure in hypersonic nozzle boundary layers. *AIAA Journal* **15** (6), 878–881.

Gaitonde, D. & Adler, M. 2022 Dynamics of three-dimensional shock-wave/boundary-layer interactions. *Annu. Rev. Fluid Mech.* In press.

Gaitonde, D. V., Shang, J. S., Garrison, T. J., Zheltovodov, A. A. & Maksimov, A. I. 1999 Three-dimensional turbulent interactions caused by asymmetric crossing-shock configurations. *AIAA journal* **37** (12), 1602–1608.

Ganapathisubramani, B., Clemens, N. & Dolling, D. 2009 Low-frequency dynamics of shock-induced separation in a compression ramp interaction. *J. Fluid Mech.* **636**, 397–425.

Huang, J., Duan, L. & Choudhari, M. M. 2022 Direct numerical simulation of hypersonic turbulent boundary layers: effect of spatial evolution and reynolds number. *Journal of Fluid Mechanics* **937**, A3.

Humble, R., Elsinga, G., Scarano, F. & Van Oudheusden, B. 2009 Three-dimensional instantaneous structure of a shock wave/turbulent boundary layer interaction. *J. Fluid Mech.* **622**, 33–62.

Jiménez, J., Hoyas, S., Simens, M. P. & Mizuno, Y. 2010 Turbulent boundary layers and channels at moderate reynolds numbers. *Journal of Fluid Mechanics* **657**, 335–360.

Klein, M., Sadiki, A. & Janicka, J. 2003 A digital filter based generation of inflow data for spatially developing direct numerical or large eddy simulations. *Journal of Computational Physics* **186** (2), 652–665.

Larsson, J. 2021 Simple inflow sponge for faster turbulent boundary-layer development. *AIAA Journal* pp. 1–3.

Larsson, J., Kumar, V., Oberoi, N., Di Renzo, M. & Pirozzoli, S. 2022 Large eddy simulations of idealized shock/boundary-layer interactions with crossflow. *AIAA J.* **60**, 2767–2779.

Lee, S. & Gross, A. 2021 Numerical investigation of sweep effect on turbulent shock-wave boundary-layer interaction. *AIAA J.* **60**, 1–19.

Lozano-Durán, A., Giometto, M. G., Park, G. I. & Moin, P. 2020 Non-equilibrium three-dimensional boundary layers at moderate Reynolds numbers. *Journal of Fluid Mechanics* **883**.

Lund, T. S., Wu, X. & Squires, K. D. 1998 Generation of turbulent inflow data for spatially-developing boundary layer simulations. *Journal of computational physics* **140** (2), 233–258.

Matheis, J. & Hickel, S. 2015 On the transition between regular and irregular shock patterns of shock-wave/boundary-layer interactions. *Journal of Fluid Mechanics* **776**, 200–234.

Padmanabhan, S., Maldonado, J. C., Threadgill, J. A. & Little, J. C. 2021 Experimental study of swept impinging oblique shock/boundary-layer interactions. *AIAA journal* **59** (1), 140–149.

Pasquariello, V., Hickel, S. & Adams, N. 2017 Unsteady effects of strong shock-wave/boundary-layer interaction at high Reynolds number. *J. Fluid Mech.* **823**, 617–657.

Piponniau, S., Dussauge, J. P., Debiève, J. F. & Dupont, P. 2009 A simple model for low-frequency unsteadiness in shock-induced separation. *Journal of Fluid Mechanics* **629**, 87–108.

Pirozzoli, S. 2010 Generalized conservative approximations of split convective derivative operators. *Journal of Computational Physics* **229** (19), 7180–7190.

Pirozzoli, S. & Bernardini, M. 2011 Turbulence in supersonic boundary layers at moderate reynolds number. *Journal of Fluid Mechanics* **688**, 120–168.

Pirozzoli, S. & Bernardini, M. 2013 Probing high-reynolds-number effects in numerical boundary layers. *Physics of Fluids* **25** (2), 021704.

Ross, D. 1953 Evaluation of the momentum integral equation for turbulent boundary layers. *Journal of the Aeronautical Sciences* **20** (7), 502–502.

Schlatter, P., Li, Q., Brethouwer, G., Johansson, A. V. & Henningson, D. S. 2010*a* Simulations of spatially evolving turbulent boundary layers up to Reθ= 4300. *International Journal of Heat and Fluid Flow* **31** (3), 251–261.

Schlatter, P., Li, Q., Brethouwer, G., Johansson, A. V. & Henningson, D. S. 2010*b* Simulations of spatially evolving turbulent boundary layers up to reθ= 4300. *International Journal of Heat and Fluid Flow* **31** (3), 251–261.

Schmisseur, J. D. & Dolling, D. S. 1994 Fluctuating wall pressures near separation in highly swept turbulent interactions. *AIAA Journal* **32** (6), 1151–1157.

Settles, G. S., Perkins, J. J. & Bogdonoff, S. M. 1980 Investigation of three-dimensional shock/boundary-layer interactions at swept compression corners. *AIAA Journal* **18** (7), 779–785.

Simens, M. P., Jiménez, J., Hoyas, S. & Mizuno, Y. 2009 A high-resolution code for turbulent boundary layers. *Journal of Computational Physics* **228** (11), 4218–4231.

Smits, A., Matheson, N. & Joubert, P. 1983 Low-reynolds-number turbulent boundary layers in zero and favorable pressure gradients. *Journal of ship research* **27** (03), 147–157.

Smits, A. J. & Dussauge, J. P. 2006 *Turbulent shear layers in supersonic flow: Second edition*. Springer New York.

Touber, E. & Sandham, N. 2009 Large-eddy simulation of low-frequency unsteadiness in a turbulent shock-induced separation bubble. *Theoret. Comput. Fluid Dyn.* **23** (2), 79–107.

Vanstone, L., Saleem, M., Seckin, S. & Clemens, N. 2017 Role of boundary-layer on unsteadiness on a mach 2 swept-ramp shock/boundary-layer interaction using 50 kHz PIV. In *55th AIAA Aerospace Sciences Meeting*, *AIAA Paper* 2017-0757.

Wenzel, C., Selent, B., Kloker, M. & Rist, U. 2018 Dns of compressible turbulent boundary layers and assessment of data/scaling-law quality. *Journal of Fluid Mechanics* **842**, 428–468.

Wray, A. A. 1990 Minimal storage time advancement schemes for spectral methods. *Tech. Rep.*. NASA Ames Research Center, Moffett Field, CA.

Xie, Z.-T. & Castro, I. P. 2008 Efficient generation of inflow conditions for large eddy simulation of street-scale flows. *Flow, Turbulence and Combustion* **81** (3), 449–470.

Xu, S. & Martin, M. P. 2004 Assessment of inflow boundary conditions for compressible turbulent boundary layers. *Physics of Fluids* **16** (7), 2623–2639.

Zhang, C., Duan, L. & Choudhari, M. M. 2018 Direct Numerical Simulation Database for Supersonic and Hypersonic Turbulent Boundary Layers. *AIAA Journal* **56** (11), 4297–4311.

Zuo, F. Y., Memmolo, A., Huang, G. P. & Pirozzoli, S. 2019 Direct numerical simulation of conical shock wave-turbulent boundary layer interaction. *Journal of Fluid Mechanics* **877**, 167–195.

List of publication acknowledging AFOSR grant support

1. Ceci, A., Palumbo, A., Larsson, J. & Pirozzoli, S. 2022a Numerical tripping of high-speed turbulent boundary layers. Theoret. Comput. Fluid Dyn. pp. 1–22.

2. Ceci, A., Palumbo, A., Larsson, J. & Pirozzoli, S. 2022b On low-frequency unsteadiness in swept shock wave / boundary layer interactions, under review. J. Fluid Mech. .

3. Ceci, A. & Pirozzoli, S. 2022 Natural grid stretching for DNS of compressible wall-bounded flows, submitted. J. Comput. Phys.

4. Di Renzo, M., Oberoi, N., Larsson, J. & Pirozzoli, S. 2021 Crossflow effects on shock wave/turbulent boundary layer interactions. Theoretical and Computational Fluid Dynamics pp. 1–18.

5. Larsson, J., Kumar, V., Oberoi, N., Di Renzo, M. & Pirozzoli, S. 2022 Large eddy simulations of idealized shock/boundary-layer interactions with crossflow. AIAA J. 60, 2767–2779.